Title

Notch1 forms nuclear transcriptional condensates that drive target gene expression.

Authors

Gregory Foran[1], Ryan Douglas Hallam[1], Marvel Megaly[1], Anel Turgambayeva[1], Yifeng Li[2], Aleksandar Necakov[1,3,*]

[1] Department of Biological Sciences, Brock University, 1812 Sir Isaac Brock Way, St. Catharines, Ontario, Canada, L2S 3A1

[2] Department of Computer Science, Brock University, 1812 Sir Isaac Brock Way, St. Catharines, Ontario, Canada, L2S 3A1

[3] Lead contact

[*] Correspondence: anecakov@brocku.ca

Summary

The Notch receptor is a titratable, context-specific counter of intercellular interactions that translates productive interactions with ligands on neighbouring cells into corresponding changes in gene expression via the nuclear localization of the Notch intracellular Domain (NICD). Using an Optogenetic Notch1 construct in combination with a live imaging transcriptional reporter and super-resolution imaging, we show that the N1ICD activates gene expression through spontaneous self-assembly into transcriptional condensates whose phase separation is driven by C-terminal Intrinsically Disordered Regions (IDR) of the N1ICD. N1ICD condensates recruit and encapsulate a broad set of core transcriptional proteins, thereby facilitating gene expression and promoting super enhancer-looping. We produced a model of Notch1 activity, whereby discrete changes in nuclear NICD abundance is translated into precise changes in target gene expression through the assembly of phase separated N1ICD 'molecular crucibles' that catalyze gene expression in a concentration-dependent manner by enriching essential transcriptional machineries at target genomic loci.

Key Words

Notch signalling, Transcription, Optogenetic, gene activation, phase condensates, transcriptional bursting, super-enhancer looping, Super-resolution microscopy

Introduction

Notch receptors constitute a family of signalling proteins that translate ligand-mediated activation by neighbouring cells at sites of direct, intercellular contact to changes in gene expression.[1–3] The Notch signalling pathway can be viewed as an integrative molecular counter of productive cellular interactions, which it translates into changes in cell-type specific target gene expression.[1–5] Notch signals are used iteratively at a wide range of distinct, context-dependent cellular decision points, and drive transcriptional programs that are highly sensitive to gene dosage.[1,6] Both deficiencies and slight perturbations of Notch signalling are associated with developmental abnormalities and numerous diseases, including T-Cell Acute Lymphoblastic Leukemia (T-ALL) in humans.[2–5,7–14]

The intracellular domain of the Notch receptor (NICD) is the primary effector of Notch signalling, and is released from the membrane through proteolytic cleavage by the gamma secretase complex in response to ligand-based activation.[3,15] Cleavage liberates the NICD from the plasma membrane, resulting in nuclear translocation.[1–3,15] Nuclear NICD binds to its DNA binding partner RBPJ at discrete genomic RBPJ-binding sites.[5,16–18] In concert with additional

factors, including MAML1, p300, and other core transcriptional machinery, NICD drives assembly of the Notch transcriptional activation complex, thereby activating Notch target gene expression.[3,6,19,20] A fundamental unresolved question regarding Notch signalling is how increases in nuclear NICD abundances regulate enhancer looping and translates into discrete changes in transcriptional output across multiple target genes.

Recent investigations have shown that enhancer-looping is regulated by proteins that undergo liquid-liquid phase separation (LLPS), leading to the formation of phase condensates.[21–23] Phase condensates are dynamic, motile, and self-organizing structures that can spontaneously form and reorganize themselves, and have the capacity to undergo fusion with neighbouring condensates.[24–26] The ability for proteins to participate in LLPS, and thereby form phase condensates, is driven by the presence of intrinsically disordered regions (IDR).[27,28] The formation of a specialized subset of nuclear phase condensates, termed transcriptional condensates, has previously been linked to the regulation of target gene expression, enhancer looping, and increased local concentrations of transcriptionally active proteins.[29,30] In addition, several transcriptional regulators, including YAP, TAZ, MED1, P300, and BRD4 have been shown to phase separate into transcriptional condensates.[29–33]

Here we performed *in silico* analysis of the Notch1 NICD (N1ICD) and identified an IDR in the C-terminal tail using several different predictive models.[34,35] Previous studies have provided strong evidence that the C-terminal domain of Notch1 is essential to drive high levels of Notch target gene expression in multiple contexts.[36,37] However, the mechanism through which the C-terminal tail of Notch1 potentiates gene expression has not been resolved. Using purified N1ICD we demonstrated that N1ICD phase separates in a salt and concentration-dependent manner. In addition, we demonstrate that endogenous N1ICD forms intranuclear phase condensates that are susceptible to phase emulsification.

We further validated these results by investigating the capacity of N1ICD to form functional transcriptional condensates by generating several novel molecular tools to simultaneously control and monitor the activity of Notch1 in living human cells. The first of these tools is an engineered Optogenetic Notch protein construct (OptoNotch) that provides the ability to precisely titrate intranuclear levels of transcriptionally active N1ICD in real-time. By employing Opto-Notch, we show for the first time that the N1ICD spontaneously self-organizes into transcriptionally active phase condensates that recruit and encapsulate several key factors necessary for transcriptional activation of canonical Notch1 target genes. We also demonstrate that the spontaneous self-assembly of these transcriptional condensates is dependent upon the presence of the intrinsically disordered C-terminal N1ICD tail. We also developed a fluorescent transcriptional reporter system that provides a high-fidelity, quantitative, temporal read-out of the formation of nascent transcriptional foci of the Notch1 target gene Hes1 in live cells. By employing this tool, we uncovered a novel regulatory mechanism in which N1ICD self-associates into hollow spherical condensates that resist transcription-driven dissociation, increasing the duration of transcriptional bursting.

In addition, we demonstrate that Notch1 transcriptional condensate assembly drives super-enhancer looping between the Notch-dependant c-Myc (Myc) enhancer (NDME) and the Myc promoter, located >1.7 megabases away, and directs concomitant expression of the Myc protooncogene; this establishes a mechanism of Notch1-dependent super-enhancer looping in human T-ALL cells via phase condensate formation.[7–9,38]

Results

Human N1ICD exhibits phase condensate/LLPS behaviour

To assess the potential of the N1ICD to undergo phase condensation, we first performed *in silico* analysis using an atomic resolution model of the human N1ICD generated with AlphaFold.[39,40] AlphaFold generated a predicted structure with a high degree of disorder in the

c-terminal tail of the N1ICD (Arginine2020 to Lysine2555, Figure 1A, Blue), which lies immediately downstream of the highly ordered Ankyrin repeats (Figure 1A, green, Figure S1). We then performed *in-silico* analysis using a suite of publicly-available bioinformatic tools commonly employed in LLPS prediction.[24] These included Prediction of intrinsic disorder by IUPRED, PAPA and PLAAC, Prediction of prion-like domains (PLD) by PLAAC, Net charge per residue (NCPR), Fraction of charged residues (FCR), and hydrophobicity analysis (CIDER) of N1ICD (Figure 1A).[34,35,41,42] Consistent with a previous study that identified an important role for an IDR in the Notch1 RBPJ-associated motif (RAM) for transcriptional activation complex assembly through charge-patterning-mediated Notch1/RBPJ interaction.[43] In addition to the RAM domain, our analysis provided preliminary evidence to support the hypothesis that the carboxy-terminal tail containing the transcriptional activation domain (TAD), which plays a critical role in Notch1-mediated transcriptional activation, is highly disordered and can undergo LLPS (Figure 1A).[43,44] Collectively, these results led us to hypothesize that N1ICD can undergo LLPS to form phase condensates.

We tested this hypothesis experimentally by performing *in vitro* analysis on purified N1ICD::GFP protein. Titration of purified N1ICD::GFP protein resulted in the formation of phase-separated droplets starting at a concentration of 20µm, where with increasing concentration, we observed an increase in the average size of N1ICD::GFP droplets from 1.69µm^2(+/-6.09) to 9.35µm^2(+/-21.1) to 16.1µm^2(+/-31.1), respectively (Figure 1C/E). As further evidence of phase condensation, N1ICD phase separation exhibited a dependence upon salt concentration in that condensate size was proportional to the amount of salt present, where we observed an average condensate size of 5.34µm^2(+/-14.6), 8.49µm^2(+/-22.9), and 12.4µm^2(+/-27.9) for 50, 150, and 250mM NaCl, respectively, while we observed no N1ICD condensate formation in the absence of salt (0mM NaCl, Figure 1D/F). Consistent with previous studies that reported the formation of hollow phase condensates at elevated salt concentrations, intra-condensate cavities could be observed at higher NaCl concentrations (Figure 1G).[45,46] Consistent with LLPS, we also observed a complete loss of N1ICD::GFP droplets almost immediately after treatment with 1,6-hexanediol, a well-characterized aliphatic alcohol used to dissolve protein phase condensates (Figure 1H).[47]

Endogenous N1ICD forms intranuclear phase condensates

We next investigated the formation of N1ICD phase condensates in human cells by performing fluorescent immunohistochemistry against the N1ICD using two highly validated antibodies, referred to as DSHB and ATLAS, that recognize distinct epitopes in the C-terminus of the N1ICD (Figure 1I). Consistent with N1ICD phase condensation in the nuclei of human cells, our analysis revealed prominent and widespread nuclear N1ICD foci that exhibited statistically similar distributions in both number per nuclei, DSHB 36(+/-44) and ATLAS 34(+/-48), as well as volume, DSHB 0.141µm^3(+/-0.201) and ATLAS 0.149µm^3(+/-0.214)(Figures 1I/J/K). Considering the comparable performance of both Notch1 antibodies, all subsequent fluorescence immunohistochemistry against Notch1 was performed with the ATLAS Anti-Notch1 antibody owing to compatibility with the data available from the Human Protein Atlas project.[48] To further characterize the concentration dependency of endogenous N1ICD phase-separated droplets/condensates, we next investigated the formation of N1ICD phase condensates *in vitro* in several human cell lines. Four cell lines were selected on the basis of RNA Expression data from the Human Protein Atlas to investigate the relationship between Notch1 abundance and propensity for phase condensate formation over a range of Notch1 protein expression levels.[48] These cell lines included: SH-SY5Y, HEK293, HeLa, and U2OS cells, which exhibit increasing levels of Notch1 expression in the order presented (Figure 1L).[48] Consistent with the relative endogenous Notch mRNA level data from the Human Protein Atlas, we observed an increase in total cellular Notch1 protein abundance across the four human cell lines, 130(+/-31.3), 216(+/-66.9), 268(+/-149), and 370(+/-98.9) fluorescent intensity units respectively for SHSY5Y,

HEK293, HeLa, and U2OS cells, as well as an increase in the volume of Notch1 nuclear phase condensates, 0.0511μm^3(+/-0.222), 0.1586μm^3(+/-0.232), 0.206μm^3(+/-0.267), and 0.441μm^3(+/-0.618) respectively for SHSY5Y, HEK293, HeLa, and U2OS cells (Figure 1M/N). Consistent with our *in vitro* data for N1ICD, this result provides strong evidence that Notch1 nuclear foci are concentration-dependent in their formation and size. Importantly, treatment with 5% 1,6-Hexanediol resulted in a near-complete loss of endogenous nuclear N1ICD condensates, which was reflected by a reduction in both the number, 38.7(+/-29.6) to 0.872(+/-1.77), and size of nuclear N1ICD foci, 0.146μm^3(+/-0.220) to 0.0595μm^3(+/-0.736), providing evidence that endogenous Notch1 forms 1,6-Hexanediol-soluble intranuclear phase condensates in human cells (Figure 1O/P/Q).

Development of an Optogenetic Tool to Control Notch activity

To further characterize N1ICD phase condensates, we next developed a novel tool that would allow for pulse-chase experiments on N1ICD nuclear translocation in living human cells. To do so, we adapted an existing Split Tobacco Etch Virus (TEV) protease-based optogenetic cleavage system to generate transgenic constructs that provide precise light-gated control over the release of ectopically expressed N1ICD::GFP from the plasma membrane upon light exposure; henceforth referred to as OptoNotch (Figure 2A, Figure S2).[49,50] Cells expressing OptoNotch demonstrate a significant, titratable, increase in nuclear N1ICD::GFP signal, predominantly localized to discrete nuclear foci after blue light illumination (Figure 2B, M.1). As a control for non-specific cleavage and aberrant nuclear localization, we designed an OptoNotch construct with a point mutation in a key residue in the canonical TEV cleavage sequence essential for TEV-mediated cleavage, named OptoNotch^{mut}.[51] In contrast to OptoNotch, OptoNotch^{mut} exhibits no increase in Nuclear N1ICD::GFP, remaining tethered to the plasma membrane despite continuous blue light illumination (Figure 2C). We next measured the kinetics of light-induced N1ICD::GFP nuclear translocation and observed a significant increase in N1ICD::GFP within the nucleus over 30 minutes with a concomitant appearance of prominent nuclear N1ICD::GFP foci starting at 8 minutes post-blue light activation (Figure 2D). OptoNotch^{mut} does not exhibit an observable accumulation of N1ICD in the nucleus regardless of illumination status or duration (Figure 2D). This data demonstrates that Opto-Notch provides precise, titratable, light-gated control over the nuclear translocation of N1ICD::GFP. We next quantified the cleavage status of OptoNotch by Western blot, where we observed a near-complete light-gated cleavage of full-length, plasma membrane-tethered OptoNotch, resulting in the production of the expected ~160 kDa fragment following exposure to blue light (Figure 2E). We also observed a small degree of cleavage occurring in the absence of light and attribute this result to the exquisite sensitivity of the CRY2/CIBN interaction to blue light, where the collection of Western blot samples may have resulted in the exposure of blue light sufficient to drive aberrant cleavage (Figure 2E).[50,52,53] Our live imaging data confirm this likelihood, as all the cells we imaged exhibited clear light-gated responsiveness regarding nuclear translocation of cleaved N1ICD::GFP (Figure 2B). To validate the functionality of OptoNotch in driving Notch target gene expression, we next quantified the impact of OptoNotch activity on the expression of Hes1, a well-characterized Notch1 target gene.[54] Following blue light activation of OptoNotch, we observed a concomitant increase in Hes1 expression in HEK293 cells over the course of one hour, with a significant increase in Hes1 mRNA levels observable after 15 minutes of blue light activation and a further significant increase after 45 minutes (Figure 2F). To test the orthogonality of OptoNotch with respect to endogenous Notch signalling, we pharmacologically inhibited endogenous Notch activity with a gamma-secretase inhibitor (GSI) with simultaneous OptoNotch activation. We observed a decrease in Hes1 expression with GSI treatment of HEK293 cells. Consistent with OptoNotch function being orthogonal to endogenous Notch activity, OptoNotch is insensitive to GSI treatment and can rescue Hes1 expression independent of endogenous Notch activity (Figure 2G). Overall, our data establishes OptoNotch

as a functional light-gated tool capable of regulating Notch activity through the nuclear localization of N1ICD::GFP, and concomitant expression of the Notch target gene Hes1, even in the absence of endogenous Notch signalling. Importantly, we also observed the formation of prominent nuclear N1ICD::GFP foci that may represent phase-separated condensates.

Biophysical characterization of N1ICD nuclear foci

To determine whether nuclear N1ICD::GFP foci undergo phase separation, we treated HEK293 cells with OptoNotch with 5% 1,6-Hexanediol and observed a near-complete loss of all nuclear foci immediately following treatment, with an average of 29.7(+/-30.1) N1ICD::GFP phase condensates per cell reduced to 0.6(+/-0.8) N1ICD::GFP phase condensates per cell (Figure 3A/B). We next sought to test the hypothesis that N1ICD forms nuclear phase condensates by characterizing the biophysical properties of phase-separated nuclear N1ICD::GFP foci using Fluorescence Recovery After Photobleaching (FRAP).[26,55–57] Using this approach, we observed that following complete photobleaching of individual nuclear foci, there is a 46%(+/-14) mobile fraction of the total N1ICD::GFP signal within a single focus over 300 seconds. We also determined that N1ICD::GFP exhibited a time-to-half recovery of 24(+/-5) seconds within individual nuclear foci (Figure 3C/D, M.2). In addition, a key characteristic of LLPS condensates is their ability to undergo inter-condensate fusion.[21,25,26] Consistent with this feature, we observed multiple instances of intra-nuclear N1ICD::GFP condensate fusion, where several condensates fuse over time (Figure 3E, M.3). By quantifying the intensity of individual condensates, we observed that the fluorescence of post-fusion condensates equates to the sum of the fluorescence of the individual foci prior to fusion (Figure 3S).

The lack of complete recovery following photobleaching suggests that there may exist pools of N1ICD::GFP that exhibit differential exchange kinetics. This prompted us to ask whether incomplete recovery is driven by intra-focus heterogeneity, where select sub-domains within individual condensates exhibit differential turnover rates. To address this question, we first performed live super-resolution radial fluorescence (SRRF) microscopy to achieve nanometer-scale spatial resolution of nuclear N1ICD::GFP phase condensates (Figure 3F, Figure S3).[58–60] Following SRRF, we also observed instances of N1ICD::GFP phase condensate fusion showing initial contact between two neighbouring foci leading to subsequent fusion and formation of a larger condensate (Figure 3G).

SRRF revealed that N1ICD::GFP phase condensates form hollow spheres, which, when subjected to photobleaching, exhibit only an eighteen percent (18+/-7%) mobile area relative to the original area over 10 minutes (Figure 3H/J/O). This result demonstrated that initial recovery is non-uniform across the surface of individual phase condensates, implying that there exist heterogeneous N1ICD::GFP interactions within individual phase condensates such that subdomains of condensates exhibit differential exchange kinetics with their surrounding environment. Next, to test the intra-phase condensate dynamics of individual foci, we bleached only a sub-region of single N1ICD nuclear phase condensate, along with the surrounding area, to minimize the effect of the influx of soluble N1ICD::GFP. We found that a sub-population of molecules within a single-phase condensate exhibits intra-focus movement at an approximate speed of 125 nm/min (Figure 3I/K/R). Thus, our FRAP data support a model in which N1ICD::GFP molecules can move dynamically through nuclear foci and that discrete regions within individual foci exhibit heterogeneous N1ICD::GFP exchange kinetics.

We observed that N1ICD::GFP phase condensates undergoing growth and decay phases where individual condensates show the capacity to gain and lose N1ICD::GFP molecules (Figure 3L/M/N/, M.4). In addition, we observed core formation following initial condensate seeding, showing that core formation is a function of titrating local N1ICD::GFP levels (Figure 3P). We then sought to determine the relationship between condensate volume and width of N1ICD::GFP shell signal. With this, we demonstrated that the addition or loss of

N1ICD::GFP modulates the total volume of condensates, with the width of N1ICD::GFP signal staying constant over condensate volume (Figure 3T).

These results provide strong evidence for the organization of N1ICD::GFP into nuclear phase condensates that possess dynamic intra and inter-condensate molecular movement.

N1ICD scaffolds the assembly of functional nuclear multiprotein transcriptional condensates

A growing body of research has advanced a model in which transcriptional condensates play an instrumental role in regulating gene expression through the ordered association of transcriptional machineries.[27–33] Therefore, seeing that nuclear N1ICD foci exhibit properties consistent with LLPS condensates and that these foci are organized into a surface-shell morphology consistent with the formation of hollow condensates.[45,46] We next sought to determine whether N1ICD::GFP foci represent a functional cohort of N1ICD responsible for activating target gene expression. To test the hypothesis that N1ICD::GFP forms functional transcriptional condensates, we first performed an array of pairwise fluorescent immunohistochemical stains in GSI-treated OptoNotch-activated cells to determine whether N1ICD::GFP condensates contain core components of the Notch transcriptional activation complex (RBPJ, p300), the general transcriptional machinery, including Med1, RNAPol2, BRD4, and nascent RNA transcripts (BRDUTP). Consistent with functional transcriptional condensates, we observed that N1ICD::GFP nuclear condensates co-localize with canonical Notch Protein interactors RBPJ and p300, transcriptional regulators Med1 and BRD4, RNA POLII, as well as nascent transcribed mRNA (Figure 4A/B). Although most condensates did not show a complete co-localization between N1ICD and any of the components examined, we observed that more than 85% of N1ICD::GFP foci contained some level of RBPJ, p300, MED1, and RNA POLII, while ~ 80% of foci contained recently transcribed RNA, and approximately 69% of foci contained BRD4 (Figure 4C/D, Figure S4). Next, we sought to build an association map to determine the relative distance between a protein of interest and the edge of the N1ICD condensate using SRRF microscopy. Consistent with previous results showing incomplete co-localization, we observed that proteins within N1ICD::GFP condensates do not form a uniform layer (Figure 4E).

Interestingly, N1ICD::GFP forms an exterior shell encapsulating the transcriptional machinery (Figure 4E/F). Our findings demonstrated an ordered distance of protein enrichment where RBPJ showed the closest proximity to the Notch1::GFP shell, followed by p300 with Med1, BRD4, and nascently transcribed RNA being the most distant from the shell being more central within a N1ICD::GFP transcriptional condensate. RNA POLII appeared to have the most diffuse and variable distance from the edge of N1ICD::GFP foci (Figure 4E/F).[7–9,61–64] Consistent with RNAPolII localization, upon 30-minute pulse-chase staining with BrdUTP, we observed significant amounts of nascent RNA centrally localized within N1ICD::GFP phase condensates (Figure 4E/F, Figure S4), providing evidence that nuclear N1ICD::GFP foci represent transcriptionally active condensates. Consistent with this observation, we also observed that N1ICD::GFP condensates co-localize with both RNA, as demonstrated by staining with a live RNA dye (Figure 4G), and nascent mRNA transcripts of Notch target genes Hes1, Hes5, and Hey1 (Figure 4H, Figure S5).[3,5,12,17,65] These results demonstrate that N1ICD::GFP encapsulates transcriptional components essential to drive Notch target gene

expression inside transcriptional condensates, activating the expression of known Notch1 target genes, even in the presence of a GSI inhibiting endogenous Notch.

Analysis of the transcriptional activity of N1ICD transcriptioanl condensates

To further investigate the role of Notch1 transcriptional condensates in regulating target gene expression, we developed a novel quantitative transcriptional reporter of Notch activity compatible with live-cell imaging called Hes1-Live-RNA (Figure 5A).[66] Based upon our previous observation that OptoNotch can drive Hes1 expression, we sought to investigate the relationship between OptoNotch transcriptional foci and the frequency, amplitude, and duration of Notch1 target gene activation using our Hes1-Live-RNA system. To do so, we first benchmarked the Hes1-Live-RNA reporter by transiently transfecting our MS2 system into cells co-expressing OptoNotch and visualized the spatial distribution of OptoNotch foci with respect to sites of nascent nuclear Hes1-Live-RNA transcription sites (Figure 5B). We observed several instances of fusion of transcriptionally active condensates, alluding to the potential for individual foci to represent multiple different genomic loci with the potential to regulate several target genes simultaneously (Figure S6A). Consistent with the role of N1ICD in activating Hes1 expression, we observed co-localization between Hes1-Live-RNA foci and N1ICD::GFP (Figure 5B, and 5C-Top), in addition to a population of N1ICD::GFP foci that did not contain Hes1-Live-RNA (Figure 5B, and 5C-Bottom). With the presence of endogenous Notch and the variability of successful dual transfection, we also observed that endogenous Notch activity can activate our Hes1 reporter as we observed several instances of MS2-signal in the absence of co-localizing N1ICD::GFP signal (Figure 5D). Consistent with N1ICD concentration dependency of Hes1 transcriptional output, we observed a direct, linear relationship between the relative fluorescence of N1ICD::GFP and Hes1-Live-RNA, where increasing levels of N1ICD::GFP are positively correlated with an increase in Hes1-Live-RNA activity(Figure 5E, Pearson R^2=0.877). To circumvent limitations associated with co-transfection of multiple plasmids, mainly the limitation of having a large majority of our cells containing only one of the plasmids and not being able to control how many copies of a given plasmid any given cell receives, we generated a stable Hes1-Live-RNA HEK293 cell line.[67] Consistent with a dependence upon Notch signalling, this stable Hes1-Live-RNA cell line showed transcriptional activity under endogenous Notch Signalling levels with a mean of 17.4(+/-8.5) Hes1-Live-RNA foci per cell, which decreased to a mean of 5.1(+/-3.2) Hes1-Live-RNA foci per cell in response to GSI treatment (Figure 5F/G). Consistent with the independence of OptoNotch from endogenous Notch, we observed successful rescue of activity to a mean of 20.1(+/-9.3) Hes1-Live-RNA foci following OptoNotch activation under simultaneous blockade of endogenous Notch signalling through GSI inhibition (Figure 5F/G). Consistent with our Hes1-Live-RNA transient transfection data, we observed multiple examples of a temporal correlation between the formation of individual nuclear N1ICD::GFP foci, followed closely in time by the appearance of Hes1-Live-RNA foci at their centre (Figure 5H). In addition, the Hes1-Live-RNA foci that formed due to OptoNotch activation were significantly brighter than those formed within control cells (Figure 5I, Figure S6B/C). This further suggests that N1ICD::GFP transcriptional foci are functional in driving target gene expression and that Notch1 target gene expression is directly proportional to the total abundance of N1ICD within a transcriptional focus (Figure 5E/I). We also observed a time-dependent correlation between the intensity of N1ICD::GFP transcriptional condensates and Hes1-Live-RNA fluorescence intensity when there was co-localization between the two signals (Pearson R^2=0.684, Figure 5J). In contrast, there was no correlation in nuclear foci that contained either N1ICD::GFP or Hes1-Live-RNA alone (Figure 5K, Pearson correlation

R^2=0.091). Lastly, Nuclear N1ICD::GFP transcriptional condensates also exhibited an ability to increase the duration of Hes1-Live-RNA activity at nascent transcriptional foci from an average of 3.9(+/-0.7) minutes to an average of 18.9(+/-4.2) minutes when Hes1-Live-RNA activity is localized to an N1ICD::GFP transcriptional condensate (Figure 5F/I, Figure S6B/C). Demonstrating a direct relationship between Notch1 abundance and transcriptional output. Collectively, these data strongly suggest that increases in Notch1 activity results in increases in the size of individual N1ICD transcriptional condensates, increasing both the duration and intensity of target gene transcription.

Understanding N1ICD phase condensates dependency on the formation of the canonical Notch transcriptional activation complex.

To further identify the factors responsible for driving Notch transcriptional condensate formation, we investigated the role of Notch1 transcriptional activation complex assembly in driving Notch1 phase separation either *via* knockout of RBPJ or pharmacological disruption of the N1ICD-RBPJ complex. In contrast to wildtype and DMSO-treated cells where endogenous Notch1 formed prominent and abundant intranuclear foci, 41.371 (+/-29.38) and 43.188 (+/-31.20), we observed a significant reduction in the number of nuclear N1ICD transcriptional condensates in RBPJ knockout cells, 0.626 (+/-1.58) foci per nuclei, and when Notch transcription activation complex assembly was disrupted using CB-103, a potent and selective inhibitor of the N1ICD/RBPJ interaction, 0.304(+/-2.1) foci per nuclei (Figure 6A/B/C).[10,16] Consistent with this finding, cells with activated OptoNotch showed prominent intranuclear foci (Wildtype 30.53 (+/-30.14) or DMSO treated 32.016(+/-21.99), we saw a significant reduction in the number of intranuclear foci in both RBPJ knockout cells 0.9(+/-4.26) foci per nuclei and CB-103 treated cells 0.54(+/-0.44) foci per nuclei (Figure 6D/E/F). These data suggest that transcriptional condensate formation is stabilized and enriched when Notch can be anchored to RBPJ, but is not required for their formation as condensates can still be visualized in the absence of RBPJ.

To further test the necessity of the N1ICD:RBPJ interaction in transcriptional condensate formation, we generated two additional GFP-tagged OptoNotch alleles. These are Δ-Ankyrin N1ICD, which contains the highly disordered C-terminal portion of the N1ICD and lacks the N-terminal RAM domain and the Ankyrin repeats. The second allele is, Δ-TAD N1ICD, which contains only the RAM domain and Ankyrin repeats, essential for the physical association of N1ICD with the Notch transcriptional activation complex (Figure 6G).

Consistent with our transcriptional activation complex disruption experiments, we did not observe the formation of intranuclear transcriptional condensates in cells expressing Δ-TAD OptoNotch with cells showing only a diffuse nuclear localization of N1ICDΔ-TAD-GFP (Figure 6H/I). In contrast, in N1ICDΔ-Ankyrin OptoNotch activated cells, we see a similar result to what we observed with CB-103 treatment, and in RBPJ KO cells in that there was a significant decrease in the number of phase condensates compared to full-length OptoNotch, but there was still a persistent population of phase condensates that have formed 2.5(+/-4.09) foci(Figure 6H/I).

Due to the lack of RBPJ binding within N1ICDΔ-Ankyrin and the lack of phase condensate formation in N1ICDΔ-TAD Notch, we sought to determine whether these two truncated alleles exhibit differential mobilities compared to full-length Notch. Following photo-bleaching, ΔTAD showed a significantly larger mobile fraction of 95%(+/-4) compared to full-length Notch 46%(+/-14) and a significantly shorter half recovery time of 14(+/-2) seconds

compared to 24 seconds for full-length Notch (Figure 6J/K, M.5). However, with ΔAnkyrin, we observed a significant difference in the mobile fraction in both directions in that its 72%(+/-17) mobile fraction was significantly larger than that of the full-length Notch but also significantly lower than ΔTAD ($p<0.01$ ANOVA+Tukey post-hoc)(Figure 6J/K, M.6). For the half-recovery time, ΔAnkyrin showed a significantly slower recovery time than ΔTAD with a half-recovery time of 22(+/-5) seconds but showed no significant difference compared to full-length Notch(Figure 6J/K). This indicates that Δ-Ankyrin phase condensates are more mobile than Full-length OptoNotch, as a larger portion of the total protein is exchanged. However, it also shows that the exchange occurring in both conditions is regulated by similar interactions, as there is no difference in the half recovery time.

N1ICD Transcriptional Condensates Drive Super-Enhancer Looping at the Human Myc locus

To further investigate the role of Notch1 transcriptional condensate assembly in driving target gene expression, we employed an established model of Notch-dependent Myc proto-oncogene super-enhancer looping.[7–9,62–64] Notch transcription complex binding sites have been previously identified and characterized as the NDME, located>1.7 Mb 3′ of Myc that physically interacts with the Myc proximal promoter through enhancer looping to drive expression and concomitant proliferation in human T-ALL cells.[7–9,62–64] It is still unclear how Notch plays a role in reorganizing these distal regions, allowing for a direct effect on Myc expression following Notch binding >1.7Mb away(Figure 7A).

To address this, we sought to determine whether N1ICD::GFP transcriptional condensates are functional in driving the assembly of the Notch-dependent MYC super-enhancer and concomitant activation of MYC gene expression. Using DNA-paint to fluorescently label the MYC promoter and NDME enhancer, we observed that the Myc and NDME locus co-localize in HEK293 cells (Figure 7B/C).[68] In contrast, following Notch1 inhibition, the MYC and NDME loci become spatially distinct, demonstrating a Notch dependency of MYC-NDME super-enhancer assembly. Importantly, subsequent to OptoNotch activation in the presence of endogenous Notch1 inhibition, we observed a restoration of the co-localization between the MYC and NDME loci with OptoNotch phase condensates exhibiting 100% co-localization with intranuclear MYC-NDME loci (Figure 7B/C). Consistent with a role for the Notch transcriptional activation complex in MYC-NDME enhancer looping, we also observed that CB103 treatment led to a loss of co-localization of the MYC-NDME loci despite the presence of nuclear N1ICD phase condensates subsequent to OptoNotch activation (Figure 7B/C). When quantified, we can see a significant increase in the distance between the Myc and NDME locus when treated with GSIs or CB-103 (Figure 7D). However, when OptoNotch is present within GSI-treated cells, we see a rescue of the distance between MYC and NDME when there is coinciding N1ICD::GFP transcription condensate present (Figure 7D).

To demonstrate the ability of OptoNotch to rescue Myc expression, we performed qPCR on Myc expression in T-ALL cells, which require Notch signalling for Myc expression.[7–9,62–64] We show that following GSI treatment OptoNotch can rescue Myc expression in T-ALL cells following endogenous Notch inhibition (Figure 7E).

To further validate a dependency upon Notch for enhancer looping and direct interaction between the MYC and NDME loci, we next performed 3C-PCR, a technique commonly

employed to quantify chromatin interactions, to determine whether the formation of N1ICD::GFP transcriptional condensates brings these two distal genomic loci into close proximity to one another in both T-ALL and HEK293 cells (Figure 7F).[68–70] Our analysis revealed, similar to previous experiments, that following endogenous Notch inhibition, there is a decrease in the interaction frequency between the MYC and NDME locus compared to untreated cells (Figure 7G). This effect is then rescued when cells are OptoNotch activated while in the presence of GSI's, seeing a significant increase in the interaction frequency between the MYC and NDME compared to GSI-treated cells, but no significant difference compared to untreated cells (Figure 7G). However, the ability to form transcriptional condensates is required to recruit NDME to the MYC locus, as seen in treatment with 1,6-hexanediol, where we see a subsequent significant decrease in the interaction frequency between the Myc and NDME locus (Figure 7F/G).

Discussion

Here, we provide direct evidence that the intrinsically disordered tail of the human N1ICD drives transcriptional activation through the assembly of functional, phase-separated, intranuclear condensates in a titration-dependent manner. To do so, we developed a novel Optogenetic tool, OptoNotch, that possesses broad utility across transcription-associated proteins, which allows precise temporal and spatial control over the intranuclear levels of the N1ICD, and concomitant expression of Notch1 target genes.[49,53] Using OptoNotch, we investigated the relationship between nuclear N1ICD concentration and condensate formation. By using SRRF-based super-resolution microscopy, we demonstrate that N1ICD spontaneously self-assembles into nuclear liquid-like phase condensates.[59,60] N1ICD condensates function as molecular crucibles to encapsulate, and thereby concentrate, core transcriptional regulators and machineries, including Med1, P300, BRD4, RBPJ, and RNA Polymerase 2, which we precisely mapped to distinct regions within N1ICD condensates.

In accordance with this finding, we demonstrate that N1ICD condensates are transcriptionally active through pulse-chase labelling of nascent RNA transcripts(BrdUTP). This finding was further confirmed using single molecule RNA FISH against Hes1, Hes5, and Hey1, demonstrating that nascent target gene transcripts are spatially enriched in the centre of N1ICD condensates. In addition, we developed a novel tool to visualize and quantify the expression of Hes1 and used it to show that transcriptional output is directly proportional to the level of N1ICD in individual condensates, thereby demonstrating that the titration of Notch1 target gene expression is dependent upon the availability of intranuclear N1ICD.

Previous research has demonstrated that transcriptional condensates regulate gene expression through a non-equilibrium process that provides dynamic feedback through its RNA product, supporting a model where RNA abundance provides positive and negative feedback on transcription via regulation of electrostatic interactions.[71] Taken together, our observations show that N1ICD spontaneously self-organizes into heterogeneous spherical shells with interspersed Notch-free regions. These spherical Notch assemblies exhibit dynamic growth and reduction phases in N1ICD transcriptional condensate volume, yet do not dissolve in response to transcriptional bursting. We, therefore, speculate that N1ICD phase condensates possess entry/exit channels that allow for transit of transcriptional regulatory machinery, nucleotide substrates, and transgenic proteins into-, and nascent RNA transcripts out- of, Notch transcriptional condensates. These channels may allow for the alleviation of electrostatic repulsion driven by RNA transcript accumulation, reducing the frequency of condensate

dissolution. This provides a model that supports the observed increase in burst duration of Notch target genes inside of individual N1ICD condensates.

These results collectively provide a new mechanism by which RBPJ-associated Notch1 transcriptional condensates plays a vital role in the previously described function of Notch1 as a driver of enhancer looping, allowing for the re-organization and distribution of distinct genomic loci leading to Myc expression.[7–9,62–64]

Future directions

Recent work has demonstrated that genome topology is a critical feature of gene control and that transcriptional condensates provide an important regulatory layer to the three-dimensional organization of the genome.[72,73] Our observation of fusion between Notch transcriptional condensates implies the coalescence of multiple distinct genomic loci into single transcriptional condensates. Future studies that provide information about dynamic genomic landscapes, on a single cell level, will allow for a deeper understanding of the mechanisms that drive Notch-mediated transcriptional regulation.

We demonstrate a strategy that allows for visualization of N1ICD dynamics and downstream purification of N1ICD from human cell lysates. This technical advance provides exciting new opportunities that allow for *in-vitro* biophysical characterization of full-length N1ICD in combination with a wide variety of transcription factors, genomic enhancers, and promoters. Overall, this offers exciting new opportunities for quantitative investigation of the contribution of phase separation to transcriptional activation regulated by the Notch signalling pathway.

Limitations

This study focused exclusively on Notch1 transcriptional phase condensates, and we have not yet explored the unique features of other human and non-human NICDs, many of which differ in the presence and/or length of IDRs.[1,11] It would be interesting to make use of the diversity of Notch isoforms in order to characterize how discrete changes in IDR's potentially alter their ability to phase separate and spontaneously self-assemble into active transcriptional condensates. Furthermore, we have not investigated the role of post-translational modifications in Notch transcriptional condensate function or dynamics. Considering the large number of computationally predicted post translational modification sites identified in the N1ICD (https://elm.eu.org), we anticipate that there exists a vast unexplored landscape of Notch proteoforms. Each proteoform may represent a variant that has integrated multiple layers of cellular signalling inputs in distinct ways, and may be capable of uniquely modifying target gene transcriptional output.

Acknowledgments

This study was supported by the Natural Sciences and Engineering Research Council of Canada Discovery Grants(2018-06781). We also acknowledge Dr's Brian Cox(UofT), Frank Wippich (EMBL), Jeffery Stuart (Brock University), Rebecca MacPherson (Brock University), Tilman Borggrefe (University of Giessen), Adolpho Ferrando (NYU Langone), Yi Sheng (York University), and John Howard(University of Windsor) for various gifted reagents and help provided throughout the development of this manuscript.

Author contributions

Conceptualization, G.F and A.N.; Methodology, G.F and A.N.; Investigation, G.F., R.D.H., M.M., and A.T.; Writing – Original Draft, G.F., and A.N.; Writing – Review & Editing, G.F., R.D.H., M.M., A.T., Y.L., and A.N.; Funding Acquisition, A.N.; Formal Analysis, G.F. and Y.L.; Resources, A.N.; Supervision, A.N.

Declaration of interests

The authors declare no competing interests.

Figure 1: The Human Notch1 Intracellular Domain Exhibits Phase Condensate/LLPS Behavior Both In Isolation And Endogenously

A) Notch 1 activation complex structure determined through crystallography and subsequent superimposition of AlphaFold structure prediction of N1ICD.

B) N1ICD structural analysis.

C) Droplet assay with increasing concentration of N1ICD::GFP at 150mM NaCl.

D) Droplet assay with increasing NaCl concentration with 50μM NICD::GFP.

E) Area of condensates with different N1ICD::GFP concentration. N>5000 foci measured per condition.

F) Area of condensates with different NaCl concentration. N>500 foci measured per condition.

G) Inset from panel D showing formation of hollow cavities in in-vitro droplets at 250mM NaCl.

H) 1,6-Hexandiol treatment of 100um NICD::GFP in 150mM NaCl.

I) Endogenous Notch1 staining using ATLAS or DSHB anti-Notch1 antibody.

J) Number of foci per nucleus from panel I. N>350 nuclei measured per condition.

K) Volume of individual foci from panel I. N>10000 foci measured per condition.

L) Notch1 immunostains in multiple cell lines.

M) Total amount of Notch1 per Cell from panel L. N>400 cells measured per condition.

N) Volume of individual nuclear foci from panel L. N>3000 foci measured per condition

O) Notch1 after cells were either treated with vehicle or 1,6-Hexandiol.

P) Number of foci per nucleus within cells from panel O. N>2200 cells measured per condition

Q) Volume of individual foci from panel O. N>500 foci measured per condition.

*p<0.01 One-way ANOVA+Tukey post-hoc

$p<0.01 student T-test.

C/D/H scale bar 50μm.

G/I/L/O scale bar 10 μm.

See also Figure S1

Figure 2: Development Of An Optogenetic Tool To Control Notch1

A) Schematic of OptoNotch

B) Time series of OptoNotch activation.

C) Time series of OptoNotch^{mut} activation.

D) OptoNotch (Blue) nuclear localization compared to OptoNotch^{mut} (red). $ p<0.01 student t-test. N of 50 cells per condition. Central line-mean, darker-standard error of the mean (SEM) , and lighter shade-standard deviation (SD)

E) Western blot of OptoNotch activation.

F) qPCR of Hes1 with varying durations of OptoNotch activation.

G) qPCR of HES1 with or without GSI treatment and with or without OptoNOTCH activation.

All data acquired in HEK293

C/D scale bar 10μm.

*p<0.01 One-way ANOVA+Tukey post-hoc

qPCR graphs are mean +/- SD

qPCR has N=9 for each condition.

See also Figure S2

Figure 3: N1ICD Nuclear Foci Exhibit LLPS Properties In Living Cells

A) Vehicle or 1,6-Hexandiol treatments of OptoNotch-activated HEK293 cells. Scale bar 10μm.

B) Change in Number of Nuclear N1ICD::GFP condensates with vehicle or 1,6-Hexandiol treatment. N>1000 cell measured per condition.

C) Averaged OptoNotch FRAP curve. N= 34 N1ICD::GFP foci bleached.

D) Bleach experiments in OptoNotch activated cells.

E) Example of fusion of N1ICD::GFP foci within the nucleus of a live cell.

F) Confocal resolution compared to SRRF imaging resolution. Scale bar 10μm (left) and 500nm (right)

G) SRRF of fusion event.

H) SRRF Bleaching of singular N1ICD::GFP nuclear foci.

I) SRRF Partial area bleach of individual foci.

J) Comparison of initial to final recovery following photobleaching with intensities matched from panel H.

K) Comparison of initial to final recovery following photobleaching with intensities matched from panel I.

L) SRRFs of N1ICD::GFP condensate decreasing in size over time.

M) SRRFs of N1ICD::GFP condensate growing in size over time.

N) Overlay of the initial and final image from Panel M.

O) Overlay of the initial and final image from Panel N.

P) Formation of hollow core of N1ICD::GFP phase condensate with SRRF.

Q) Percent area recovery following photobleaching. N= 15 N1ICD::GFP foci bleached.

R) Rate of N1ICD::GFP movement within a single foci. N= 11 N1ICD::GFP foci partially bleached.

S) Total fluorescence of foci before and after fusion from panel K.

T) Comparison of N1ICD::GFP signal width to total volume of N1ICD::GFP condensate

C,Q,R,T -Central line- mean, darker shaded – SEM, lighter shade- SD

D/E Scale bar 1 µm

Panels G-P Scale bar 500nm.

All data acquired in HEK293

Figure 4: Notch1 Scaffolds The Assembly Of Functional Nuclear Multiprotein Transcriptional Condensates

A) GSI treated OptoNotch activated cells stained for either RNAPOLII, RBPJ, p300, Med1, BRD4, or mRNA (BRDUTP).

B) Inset of individual N1ICD::GFP condensates from panel A. scale bar 2 µm.

C) Total nuclear co-localization of N1ICD::GFP with co-staining component. N>100 nuclei measured per condition.

D) Venn diagrams of the proportional number of nuclear N1ICD::GFP phase condensates (Green) that contain the given co-staining protein, in relation to the total amount of co-staining protein (Black). N>500 nuclei measured per condition.

E) SRRF images of cells from panel A.

F) Organizational heat map of an average N1ICD::GFP phase condensate greater than 500 um in diameter. N>1000 condensates measured per condition.

G) GSI treated OptoNotch activated cell treated with Live RNA dye. Scale bar 1 µm.

H) Hes1 in-situ in GSI treated OptoNotch activated cells.

A/H Scale bar 10µm.

E/F/G Scale bar 500nm.

All data acquired in HEK293

See also Figure S3/4/5

Figure 5: Analysis Of N1ICD Phase Condensates Transcriptional Bursting Behaviour.

A) Graphic of Hes1-Live-RNA construct functionality.

B) OptoNotch with Hes1-Live-RNA. Scale bar 10μm

C) Insets from panel B (Top yellow, Bottom magenta).

D) Average distance between the center of a Hes1-Live-RNA foci and the nearest N1ICD::GFP transcriptional condensate. N=16645 MS2 foci measured

E) Pearson correlation of MS2 and OptoNotch fluorescence when co-localizing. N=800 condensates measured.

F) Stably transfected Hes1-Live-RNA, either untreated, GSI treated , or GSI treated and OptoNotch activated. Scale bar 5 μm

G) Number of Hes1-Live-RNA foci in panel F. N>150 cell measured per condition.*p<0.01 one-way ANOVA+Tukey post-hoc

H) Activation of OptoNotch leading to the subsequent expression of Hes1-Live-RNA. Scale bar 2 um.

I) Time traces for intensities of N1ICD::GFP and Hes1-Live-RNA fluorescence that either co-localize or do not following initial OptoNotch activation. Black dots represent data from single trace, central line is mean, lighter shade is SD (N>10 foci measured per condition).

J) Z-scores of the relative intensity of each channel in relation to time post OptoNotch activation in co-localizing foci. Blue lines represent Pearson correlation. N = 18 foci.

K) Same as J but for non-co-localizing foci. 45 foci measured in total.

L) Histogram of duration of Hes1-Live-RNA fluorescence either non-N1ICD::GFP associated or N1ICD::GFP condensates associated. N>1200 per condition. $ p<0.01 on student T-test.

All data acquired in HEK293

See also Figure S6

Figure 6: Structure/Function Analysis Of The N1ICD With Respect To N1ICD Nuclear Transcriptioanl Phase Condensate Formation

A) Wildtype and RBPJ knockout HeLa cells stained for Notch1 and RBPJ.

B) Vehicle and CB-103 treated HEK293 cells stained for Notch1 and RBPJ.

C) Number of condensates per nucleus in A and B. N>400 nuclei measured per condition.

D) Wildtype and RBPJ knockout HeLa cells with activated OptoNotch.

E) Vehicle and CB-103 treated HEK293 cells with activated OptoNotch.

F) Number of N1ICD::GFP condensates per nucleus in D and E. N>400 nuclei measured per condition.

G) Structural layout of different truncated OptoNotch constructs.

H) Full length, ΔAnkyrin, and ΔTAD OptoNotch in HEK293.

I) Number of Foci per nucleus in H. N>700 nuclei measured per condition. $

J) Bleach experiments of nuclear ΔAnkyrin and ΔTAD OptoNotch. scale bar 2um

K) Frap recovery curves of ΔAnkyrin and ΔTAD. N>40 bleach experiments per condition. Central line mean, darker shaded SEM, lighter shade SD.

$p<0.01 student t-test comparing RBPJ KO to Wildtype and CB-103 to Vehicle.

*p<0.01 One-way ANOVA+Tukey post-hoc

A/B/D/E/H scale bar 10um

Figure 7: Notch1 Transcriptional Condensates Drive Super-Enhancer Looping At The Human Myc Locus

A) Schematic of human MYC and NDME genomic loci and subsequent Notch dependent enhancer looping

B) DNA-Paint of OptoNotch, NDME and the MYC locus in HEK293 cells treated with vehicle, GSI, GSI+N1ICD::GFP, and GSI+NICD::GFP+CB-103. Scale Bar 10um.

C) Insets from panel B.

D) Distance between the MYC and the NDME loci. N>350 MYC loci measured per condition. &,# p<0.01 One-way ANOVA+Tukey post-hoc between vehicle or GSI+NICD::GFP.

E) qPCR for Myc expression in T-ALL cells, either vehicle, GSI or GSI+OptoNotch activated.

F) 3CPCR gel electrophoresis of the Myc-NDME, Myc-NDME+80K, and MYC-MYC under vehicle, GSI, GSI+ OptoNotch, GSI+N1ICD::GFP+1,6-hexanediol either in T-ALL or HEK293.

G) 3CqPCR analyses of previously stated conditions interaction frequency. graphs are mean +/- SD. $p<0.01 student t-test between the Myc-NDME and Myc-NDME+80k within a condition. N=9 for each condition

*p<0.01 One-way ANOVA+Tukey post-hoc

METHODS

Cloning

OptoNotch constructs (OptoNotch (Full-length N1ICD [aa1779-2555]), OptoNotch^{mut} (mutant TEV cleavage sequence), OptoNotchΔTAD [aa1779-2169], OptoNotchΔankyrin [aa2170-2555], Cry2-cTEV) were generated by PCR and Gibson assembly to be subsequently sub-cloned into a modified MXS chaining vector containing a CMV promoter and BGHpa Tail. [74]

OptoNotch comprises two separate proteins: one containing Cry2PHR, a protein that, when illuminated with blue light, will interact with its binding partner CIBN, followed by the c-terminal half of the TEV protease[49,50]. The complementary synthetic protein partner contains a Lyn11 membrane tether, CIBN, the optogenetic partner of Cry2PHR, the N terminal portion of the TEV protease, an AsLOV2 domain, which acts to sequester the TEV cleavage sequence while in the dark to reduce any potential dark activity, directly on the N-terminal to a TEV cleavage sequence (ENLYFQ/S), immediately followed by the N1ICD, carrying a C-terminal mEmerald green fluorescent protein tag[52,75]. For the generation of OptoNotch^{mut} a key residue in the canonical TEV cleavage sequence essential for TEV-mediated cleavage was mutated ENLYFQ/S mutated to ENLRFQ/S, which is not susceptible to TEV-induced cleavage[51].

Sequences for PCR and cloning reactions were acquired from TetO-FUW-N1ICD (addgene,61540), MXS_bGHpa (addgene,62425), pCMV-NES-CRY2PHR-TevC (addgene,89877), pCMV-TM-CIBN-BLITz1-TetR-VP16 (addgene,89878), MXS_CMV (addgene,62417) , Lyn11-GFP-CIBN (addgene,79572), and mEmerald-N1 (addgene,53976) .

Hes1-Live-RNA system involves two components: 1) A functional fragment of the human Hes1 promoter, which drives the expression of RNA transcripts carrying 24 copies of the MS2 stem-loop sequence, and 2) a constitutively active cytomegalovirus (CMV) promoter driving the expression of an MS2-coat protein (MCP) ::mScarlet fusion protein [65,66].

The Hes1 promoter sequence was made from isolated ShSy-5Y genomic DNA using primers based on the known sequence of the human Hes-1 promoter[65].

Hes1-Live-RNA (PiggyBac 5" LTR [Hes1-MS2-bGHpa/CMV-mScarlet-MCP-bGHpa/CMV-Puromycin-bGHpa] PiggyBac 3' LTR) was constructed through a combination of iterative restriction digestions and T4 reactions using MXS cloning as well as Gibson assembly for the final construction of all components into a final plasmid[67].

The PiggyBac Transposase and pENTR-MCP vectors were gifted by B.Cox (UofT), MS2 24x stem-loop sequences was gifted by Frank Wippich (EMBL), and pmScarlet_C1 was acquired through addgene (85042). All primers used for cloning can be seen in supplementary table 1.

Cells used

HEK293 cells (Cedarlanelabs, CRL-1573; RRID:CVCL_0045), HeLa cells(RRID:CVCL_0030) were gifted from Dr. Jeffery Stuart at Brock university, Dr. Rebecca MacPherson gifted SHSY-5Y cells at Brock university, HeLa RBPJ KO cells were gifted from Dr. Tilman Borggrefe (University of Giessen)[16], and T-ALL CUTTL1(RRID:CVCL_4966) cells were gifted from Dr. Adolpho Ferrando (NYU Langone). U2OS(RRID:CVCL_0042) cells were gifted from Dr. Sheng (York university).

Cell culture protocol

All cells were cultured in PlasMax media supplemented with 1% pen/strep and 2.5 % fetal bovine serum.[76] Cells were either cultured on a 35mm collagen coated 1.5 coverslip well plates (P35GCOL-1.5-14-C,matek) for live imaging, in-situ hybridization, mRNA isolation and DNA paint experiments; a 24 well uncoated 1.5 coverslip well plate (P24-1.5H-N, Cellvis) for immunohistochemistry, or a 10cm dish for western blot and protein purification. Cells were grown at 37°C with 5% CO2 in a humidified incubator.

Cell treatments

Transfection: For adherent cells, cells were transfected with Lipofectamine 3000 (Life Technologies, L3000008) following manufacturer's instruction, and cells were either live imaged or fixed 24 hours post-transfection. For CUTTL1 cells, cells were transfected using a Neon Transfection System (ThermoFisher) for 3x10ms pulses at 1350 mV. For light-sensitive experiments following transfection, plates were subsequently wrapped in tinfoil and placed in a blackened box inside the incubator.

BRDUTP Transfection: Cells to be immunostained for BRDUTP (Millipore, B0631) were initially treated and transfected with OptoNotch on day 0. The following day, cells were transfected with BRDUTP, and cells were then allowed to incubate for 30 minutes, at which point, cells were fixed and immunostained.

Drug treatments: Cells treated with either CB103 (Selleckchem, S9719) or compound E (ABcam, ab142164) were treated with a 1μM final concentration for 24 hours prior to fixation. If cells were to be transfected and treated, cells were initially treated with compound E or CB103 for 2 hours before transfection, transfected and then either live imaged the following day or fixed the following day. For 1,6-hexanediol (Millipore-Sigma, 240117-50G) treatments, cells were supplemented with 10% of the total volume of the culture media with preheated 50% 1,6-Hexandiol immediately prior to fixation for immunohistochemistry and 3CqPCR or following initial imaging for live cells while still on the microscope.

Stable cell production: Hes1-Live RNA stable cells were transfected with PiggyBac [Hes1-MS2-bGHpa/ CMV-mScarlet-MCP-bGHpa/ CMV-Puromycin-bGHpa] along with PiggyBac transposase into HEK293 cells and following 24 hours cells were treated with 1ug/ml puromycin for 2 weeks changing the media every 2 days. Cells were then taken off of puromycin for 2 weeks, followed by 2 more weeks of treatment to remove remaining non-Stably transfected cells.

Nuclei counter staining for live imaging: Cells were treated with 1ul Hoechst 33342 (thermos, H3570) per 1ml of media for 5min at 37°C prior to initiating imaging experiments.

Live RNA dye imaging: Cells were treated with F22 RNA dye, which was synthesized by Dr John Howard (University of Windsor), at 1μM for 5 minutes and subsequently washed off with fresh media 3 times prior to live cell imaging.[77]

Qpcr

RNA was extracted with the Total RNA Purification Kit (Norgen,17200). cDNA was then synthesized from the isolated RNA with iScript™ cDNA Synthesis Kit (Bio Rad) and quantified on a nanodrop lite. Transcripts were amplified with iQ™ SYBR® Green Supermix (BioRad), and quantitative PCR was performed on an CFX96 real-time qPCR machine (Bio-rad). Primers used can be seen in Table S1. qPCR data was analyzed as fold changes in expression with three separate housekeeping genes as controls.

Antibodies

The following antibodies were purchased from commercial sources : Rat Anti-Notch1 (DSHB, BTAN-20; RRID:AB_2153497, 1:50) Rabbit- Anti-Notch (Atlas,HPA067168; RRID:AB_2685795,1:500), Rabbit Anti-RBPJ (Atlas, HPA060647; RRID:AB_2684337, 1:500), Rabbit Anti- RNAPolII (Atlas, HPA037506; RRID:AB_10672597, 1:500) ,Mouse Anti- BRD4

(Atlas, AMAb90841; RRID:AB_2665685, 1:500), Rabbit Anti- MED1 (Atlas, HPA052818; RRID:AB_2681962,1:500), Rabbit Anti- P300 (Atlas, HPA004112;RRID:AB_1078746, 1:500), Mouse Anti- BRDUTP (DSHB,G3G4; RRID:AB_1157913,1:1000), Anti-Mouse-568 (invitrogen, A11031 ,1:1000), Anti- Rat-568 (invitrogen, A11077,1:1000), Anti- Rabbit-568 (invitrogen, A11011 ,1:1000), Mouse Anti-DIG-568 conjugated (Jackson immuno-research,1:500)

SDS-PAGE and western blot analysis

Unless otherwise stated, samples were lysed in ice-cold RIPA buffer containing 1X protease and phosphatase inhibitors (10 mM phenylmethylsulfonyl fluoride, 1 mM aprotinin, 1 mM sodium orthovanadate and 1 mM sodium fluoride). Samples were homogenized by sonication and briefly centrifuged at 13,000 rpm to remove cellular debris. The concentrations of the resulting protein lysates were determined using the BioRad DC Protein Assay Kit as per manufacturer's protocol. Unless otherwise stated, all SDS-PAGE was performed on protein lysates using 10% resolving gels and 4% stacking gels run at 80V for 15 minutes and 110V for 90 minutes. Proteins were then transferred onto 0.2 µm nitrocellulose membranes at 50V overnight (~16 hours) on ice. Membranes were blocked for 1 hour in a blocking buffer (5% non-fat dry milk in PBS) with constant agitation. Primary antibodies were administered at a dilution of 1:1000 in blocking buffer and incubated overnight at 4°C with constant agitation. Following three washes with PBS + 0.1% Tween 20, membranes were blocked again with blocking buffer for 1 hour and then probed with secondary antibody at a dilution of 1:5000 in blocking buffer for 1 hour at room temperature. To visualize HRP-conjugated secondary antibodies, membranes were probed for 5 minutes with clarity western enhanced chemiluminescence blotting substrate and imaged with the ChemiDoc Imaging System (Bio-Rad).

Immunohistochemistry

Cells were fixed in 4% paraformaldehyde in phosphate-buffered saline (PBS) for 10min at room temperature (RT). After three washes in PBS for 5min. Cells were permeabilized with 0.2% triton X100 (Sigma Aldrich, X100) in PBS for 2 min at RT. Following three washes in PBS for 5 min, cells were blocked with either 2% skim milk for antibodies acquired from the DSHB, ABCAM or Invitrogen, or in 4% fetal bovine serum for antibodies acquired from ATLAS antibodies for at least 40 minuntes at RT. Primary antibodies were incubated at the previously stated dilution in there given blocking serum for 24 hours at 4^{o}C. Cells were then washed with PBS+0.1% tween (PBST) 3 times. The associated secondary antibody was then incubated on cells at their designated dilution for 2 hours at room temperature in the dark. Cells were washed three times with PBST, and one final 10 min wash in PBS containing 1:1000 Hoechst 33342. Cells were then placed in Vectashield hardset (BioLynx Inc., VECTH1400) and imaged.

In-situ probe synthesis

To produce in-situ probes, cDNA was created identically to our qPCR protocol with the following changes, synthesis was done for 4 hours instead of 1 hour and ethanol precipitation was carried out overnight instead of over the span of 2 hours.. Following cDNA synthesis probe synthesis was carried out as previously described.[78] With DIG-UTP (SIGMA, DIGUTP-RO), T7 RNA polymerase and RNAPol Reaction Buffer (NEB,M0251) used in our reaction.

In-situ hybridization

Cells were treated with GSI and transfected with OptoNotch. 24 hours post-transfection, cells were fixed and permeabilized identically to immunohistochemical experiments. After fixation cells were placed in hybridization buffer (5% dextran sulfate, 50% formamide, 5× SSC , 100 µg/ml heparin, 100 µg/ml sonicated salmon sperm DNA (Sigma-Aldrich, cat. No. D9156),0.1% Tween-20) for 4 hours at 30 °C. Before probe incubation, probes were diluted in hybridization buffer to 1ng/µl, and the solution was incubated at 80°C for 3 minutes, then left on ice for 5 minutes. Probes were then added to cells at 60 °C and hybridized for 24 hours. The following day, cells were washed in 4x SSC for 2 minutes, 2x SSC for 30 minutes, 1x SSC for 30 minutes, and 0.1 x SSC for 20 minutes. Cells were then blocked (2% skim milk,1xPBS, 0.1% tween) for 30 minutes at room temperature. Cells were then stained identically to the immunohistochemistry protocol above.

Protein purification

Plasmids containing our full-length N1ICD OptoNotch construct were transfected into *HEK293* cells. Following 24 hours post-transfection, they were uncovered and illuminated for 1 hour. Cells were detached using trypsin-EDTA, and N1ICD::GFP was then isolated using GFP-Trap Agarose beads following the prescribed protocol (Chromotek,gta). Protein concentrations were calculated using a BSA standard curve.

Droplet assay

Purified proteins were diluted to varying concentrations in buffer containing 50 mM Tris-HCl pH 7.5 and 200 mM glycine with the indicated salt concentrations. 10 µl of each solution was loaded onto an individual uncoated 35mm Dish with a 1.5 coverslip (Mattek, •P35G-1.5-14-C) and imaged.

Molecular Dynamic simulation

Molecular dynamics simulations (MDS) were conducted using GROMACS version 2020.1 to simulate the interactions among NOTCH1, RBPJ, MAML1, and a RBPJ DNA binding site.[79,80] The complete predicted structure files of the NOTCH1 NICD (Valine 1754 to Lysine 2555 at the C-terminus), RBPJ, and MAML1 were obtained from the AlphaFold Protein Structure Database (NOTCH1: AF-P46531-F1-model_v2,; RBPJ: AF-Q06330-F1-model_v2; MAML1: AF-Q92585-F1-model_v2). [39] The structure of the human Notch1 transcriptional activation complex), which was derived using only truncated portions of each of Notch1, RBPJ, and MAML1, was extracted from the Protein Data Bank (www.pdb.org; 3v79). We then aligned the complete protein structures from AlphaFold onto the structure of the transcriptional activation complex. Initial MDS resulted in an simulation error in GROMACS due to tight entanglement. Therefore, we manually positioned the proteins in a relatively 'looser' position to successfully run the MDS. MDS steps are described as follows; we generated .gro, topol.top, and posre.itp files using a tip3p water model and amber03 force fields. We defined our simulation box using the dodecahedron box type to which we then filled with water, followed by the addition of Na^+ and Cl^- ions to reach a NaCl concentration of 0.15 M and neutralize the system. Following this, we ran energy minimization to ensure that the system had no steric clashes or inappropriate geometry during the MDS. We then performed an equilibration run for 100 ps to bring the system to a temperature fluctuating around 300 K, followed by an equilibration run for 100 ps to bring the system to a pressure of approximately 1 bar. Lastly, the "production" simulation was run for 10 ns (10000 ps). After the MDS was finalized, Visual Molecular Dynamics (VMD) was used to generate the MDS and calculate the root mean square deviation (RMSD) values relative to the starting frame.[81]

3C PCR/qPCR

3C-PCR was completed as previously described using primers previously designed to study the interaction between the Myc and the NDME locus (Table S1).[69,82] Analysis was completed using both qPCR and agarose gel images. Whereby the signal produced by MYC-NDME was divided by the signal of MYC-MYC to get a relative association rate. This was then done for the negative control MYC-NDME+80K from the same sample to act as a random association control.

DNA-paint-

DNA PAINT was completed as previously described with the following modifications.[68] Cells were instead grown on a 35 mm matek collagen-coated plate and incubated in excess volume of staining solution to remove the requirement for sealing with rubber cement. Once cells were stained, they we mounted in Vectashield Hardset and imaged. Probes were designed to target either the MYC locus (chr8: 127730000-127740000) or the NDME locus (chr8: 130175000-130185000). Myc Probe barcodes were conjugated to cy3 and NDME probe barcodes were conjugated to cy5 (IdtDNA) (Table S1).

Microscopy

All imaging was conducted on an inverted Zeiss Axio Observer spinning disc confocal microscope equipped with a Yokogawa spinning disc head and a Prime BSI 16-bit camera fitted with 4 laser lines (350-400 nm, 450-490 nm, 545-575 nm, 625-655nm) and a Zeiss Direct FRAP FLIP Laser Manipulation for Axio Observers (Zeiss,423635). Most imaging was completed with a 40x 1.4 NA Plan Apochromat oil objective, except for droplet assay imaging which used a 20x 0.8 NA Plan Apochromat air objective. Imaging was conducted on a stage-fitted dark box incubator with CO2 and temperature regulation to allow live imaging at 37°C with 5% CO2. Image analysis was then carried out on ImageJ (RRID:SCR_002798) as described below.[83]

Image analysis

Phase condensates volume and counting: Nuclei of individual cells were isolated, using Hoescht as an ROI to isolate signal only emitting from the nuclei of individual cells. We then applied the 3d object counter function in ImageJ to determine the number and volume of each phase condensate within a given nucleus.

Nuclear localization rate: We first isolated nuclear proteins as described above in *Phase condensates volume and counting*. The change in Nuclear GFP signal was measured at each time point and then normalized to time 0 within each condition, and these values were then averaged across multiple trials to determine rate of N1ICD::GFP nuclear translocation following OptoNotch activation.

Co-localization: We first Isolated for nuclear proteins, as done above in *phase condensates volume and counting*, we then calculated Manders co-efficiencies for N1ICD::GFP signal and the given co-stain to determine total nuclear localization between the two in relation to total nuclear N1ICD::GFP signal. We then measured the total amount of fluorescence of the co-staining protein within the nucleus and then measured the amount of signal that is coinciding with nuclear N1ICD::GFP and represented that as a fraction of total nuclear protein. To then get

the ratio of N1ICD::GFP phase condensates that contained some level of a co-staining protein we then took a total count of the number of nuclear N1ICD::GFP phase condensates and compared that to the number of N1ICD::GFP phase condensates that contained some level of co-staining protein.

Bleaching- Using the Zeiss Direct FRAP FLIP Laser Manipulation for Axio Observers, one of two different conformations of bleaching areas were used to either: bleach a single Nuclear N1ICD::GFP phase condensates, or bleach a partial area of a single phase condensates along with the surrounding area. Bleached areas were measured every 2 seconds following bleaching or imaged every 30 seconds for SRRF data collection. Bleach Frap kinetics were fit using R to the first order kinetic In quantifying our FRAP data, we fit the average bleach kinetic to the equation

$$f\ (t) = A\ (1 - e^{-t/\tau})$$

where A represents the mobile fraction, τ is the time constant, and t is the time post-bleach.

SRRF image acquisition-To acquire SRRF data the capture field of the camera was reduced to 400x400 pixels and 200 images were acquired at 100 % laser power with an excitation time of 500 µs. SRRF images were then calculated using the NANOJ SRRF plugin in ImageJ.[59,60] To Validate our SRRF outputs, a random subset of 250 images across all conditions were chosen to be run through squirrel analysis for accuracy.[58]

SRRF arrangement determination- After isolating for individual Nuclear N1ICD::GFP condensates ROI's were drawn around all unique fluorescence signal of the co-staining protein within a condensate. The minimal distance between the center of mass of each ROI and the nearest edge of N1ICD::GFP shell was measured over trials. All measurements were then run through a linear kernel density operator to get a probability (Density Score) of any given position in a condensate containing any of the co-staining protein. This was then repeated for each co-staining protein to produce an organization layout of the position of unique proteins within single N1ICD::GFP phase condensates.

FRAP Distance Recovery- N1ICD::GFP phase condensates that were half bleached *and imaged with* SRRF were skeletonized and the max skeleton length of each image was measured and the change in length was calculated to determine a nm/sec travel rate for proteins within a given phase condensates.

FRAP Percent Area Recovery- Individual Pre Bleach Phase condensate SRRF images were measured for total fluorescence and normalized to 1, all subsequent SRRF images total fluorescence was measured and represented as a ratio of the initial intensity as a metric of the total area recovered along individual Phase condensates. This was then repeated for each time point and averaged across trials.

Fusion- ImageJ TRACKmate was used for detecting the movement of phase condensates within a cell.[84] To isolate for fusion events phase condensates that intercepted with one another, leaving only an individual phase condensate, were isolated and subsequently quantified prior to and following fusion to determine the volume and total fluorescence over time.

Hes1-Live-RNA distance measures- Each Hes1-Live-RNA and N1ICD::GFP phase condensates in a field of view was isolated as individual ROIs. We then analyzed each ROI's center of mass and ran a comparative analysis to determine the nearest distance from each Hes1-Live-RNA foci to any given NICD::GFP phase condensates.

MS2 bursting- For this analysis, we created three separate categories of ROI's to bin OptoNotch phase condensates and Hes1-Live-RNA transcriptional foci into, these being: N1ICD::GFP phase condensates that had mScarlet signal above a detection threshold, NICD::GFP foci that did not have mScarlet signal above a detection threshold and Hes1-Live-RNA signal that was produced in the absence of OptoNotch . The ROIs were identified and tracked using ImageJ, and the maximal fluorescence intensity values for both channels within each ROI at each time point was recorded. To interpret the relationship between NICD::GFP and Hes1-Live RNA for each ROI, we produced Z-score for each channel and heat-mapped those points with respect to time post OptoNotch activation. This was done to see a correlation between the formation of NICD::GFP phase condensates and the occurrence of Hes1-Live-RNA foci. Then by recording the duration that Hes1-Live-RNA signal stayed above the threshold for any given phase condensates, we were able to determine the duration of signalling either with or without the co-occurrence of NICD::GFP.

Nearest Neighbor calculation for DNApaint- Myc and NDME nuclear foci were thresholded, and each position was labelled as the center of fluorescence for each focus. We then isolated each nuclei in the field of view and measured the minimal distance between the MYC and NDME locus within each nuclei. For the determination of the role of OptoNotch, prior to distance calculation, OptoNotch signal was used as an ROI only to include signal co-localizing with Optonotch phase condensates the distance between the MYC and NDME locus was then quantified across conditions.

Statistics and data analysis

All experiments were completed with a minimum of 3 separate technical replicates comprising 3 biological replicates (A minimum of nine total plates/wells with three plates imaged at a time repeated over three separate experiments). The individual number of measurements (N's) of each experiment is represented in the figure caption. All statistical analysis was completed using R studio.[84]

All data presented in manuscript are Mean +/- 1 Standard deviations

Supplemental Table and Movie legends

Table S1: Primers and oligonucleotides used

Movie 1 (M.1):Optonotch Activation Leading To Subsequent Nuclear Localization Of N1ICD::GFP. In HEK293 Cells Imaged Over 25 Minutes. Scale Bar 10um

Movie 2 (M.2): N1ICD::GFP Phase Condensate Bleaching Video Over 5 Minutes. Bleach Area Is Encircled In Yellow.

Movie 3 (M.3): Two N1ICD::GFP Phase Condensates Undergoing Fusion Over The Time Course Of 5 Minutes. Scale bar 1 micron

Movie 4 (M.4): N1ICD::GFP Phase Condensate Undergoing Growth Phase Showing An Increase In The Total Volume Of A Single Condensate Over 16 Minutes. Volume On Condensate Indicated In Center Of Condensate Measured For Each Frame. Scale bar 1 micron

Movie 5 (M.5): ΔTAD-N1ICD::GFP Phase Condensate Bleaching Video Over 5 Minutes. Bleach Area Is Encircled In Yellow.

Movie 6 (M.6): ΔAnkyrin-N1ICD::GFP Phase Condensate Bleaching Video Over 5 Minutes. Bleach Area Is Encircled In Yellow.

References

1. Wang, M. M. (2011). Notch signaling and Notch signaling modifiers. *The International Journal of Biochemistry & Cell Biology*, *43*(11), 1550-1562. https://doi.org/10.1016/J.BIOCEL.2011.08.005

2. Shen, W., Huang, J., & Wang, Y. (2021). Biological Significance of NOTCH Signaling Strength. *Frontiers in Cell and Developmental Biology*, *9*. https://doi.org/10.3389/FCELL.2021.652273

3. Zhou, B., Lin, W., Long, Y., Yang, Y., Zhang, H., Wu, K., & Chu, Q. (2022). Notch signaling pathway: architecture, disease, and therapeutics. *Signal Transduction and Targeted Therapy 2022 7:1*, *7*(1), 1–33. https://doi.org/10.1038/s41392-022-00934-y

4. Ninov, N., Borius, M., & Stainier, D. Y. R. (2012). Different levels of Notch signaling regulate quiescence, renewal and differentiation in pancreatic endocrine progenitors. *Development*, *139*(9), 1557–1567. https://doi.org/10.1242/DEV.076000

5. Wang, H., Zang, C., Taing, L., Arnett, K. L., Wong, Y. J., Pear, W. S., Blacklow, S. C., Liu, X. S., & Aster, J. C. (2014). NOTCH1-RBPJ complexes drive target gene expression through dynamic interactions with superenhancers. *Proceedings of the National Academy of Sciences of the United States of America*, *111*(2), 705–710. https://doi.org/10.1073/PNAS.1315023111

6. Nam, Y., Sliz, P., Pear, W. S., Aster, J. C., & Blacklow, S. C. (2007). Cooperative assembly of higher-order Notch complexes functions as a switch to induce transcription. *Proceedings of the National Academy of Sciences of the United States of America*, *104*(7), 2103–2108. https://doi.org/10.1073/PNAS.0611092104

7. Sanchez-Martin, M., & Ferrando, A. (2017). The NOTCH1-MYC highway toward T-cell acute lymphoblastic leukemia. *Blood*, *129*(9), 1124–1133. https://doi.org/10.1182/BLOOD-2016-09-692582

8. Herranz, D., Ambesi-Impiombato, A., Palomero, T., Schnell, S. A., Belver, L., Wendorff, A. A., Xu, L., Castillo-Martin, M., Llobet-Navás, D., Cordon-Cardo, C., Clappier, E., Soulier, J., & Ferrando, A. A. (2014). A NOTCH1-driven MYC enhancer promotes T cell development, transformation and acute lymphoblastic leukemia. *Nature Medicine*, *20*(10), 1130–1137. https://doi.org/10.1038/NM.3665

9. Ryan, R. J. H., et al.(2016). Notch-Regulated Enhancers in B-Cell Lymphoma Activate MYC and Potentiate B-Cell Receptor Signaling. *Blood*, *128*(22), 457–457. https://doi.org/10.1182/BLOOD.V128.22.457.457

10. Lehal, R., et al. (2020). Pharmacological disruption of the Notch transcription factor complex. *Proceedings of the National Academy of Sciences of the United States of America*, *117*(28), 16292–16301. https://doi.org/10.1073/PNAS.1922606117

11. Shah, P. A., Huang, C., Li, Q., Kazi, S. A., Byers, L. A., Wang, J., Johnson, F. M., & Frederick, M. J. (2020). NOTCH1 Signaling in Head and Neck Squamous Cell Carcinoma. *Cells 9*(12), 2677. https://doi.org/10.3390/CELLS9122677

12. Bourdon, M., Santulli, P., Doridot, L., Jeljeli, M., Chêne, C., Chouzenoux, S., Nicco, C., Marcellin, L., Chapron, C., & Batteux, F. (2021). Immune cells and Notch1 signaling appear to drive the epithelial to mesenchymal transition in the development of adenomyosis in mice. *Molecular Human Reproduction*, *27*(10). https://doi.org/10.1093/MOLEHR/GAAB053

13. Nomura, T., Nagao, K., Shirai, R., Gotoh, H., Umeda, M., & Ono, K. (2022). Temperature sensitivity of Notch signaling underlies species-specific developmental plasticity and robustness in amniote brains. *Nature Communications 2022 13:1*, *13*(1), 1–14. https://doi.org/10.1038/s41467-021-27707-5

14. Severson, E., Arnett, K. L., Wang, H., Zang, C., Taing, L., Liu, H., Pear, W. S., Liu, X. S., Blacklow, S. C., & Aster, J. C. (2017). Genome-wide identification and characterization of Notch transcription complex-binding sequence paired sites in leukemia cells. *Science Signaling*, *10*(477). https://doi.org/10.1126/SCISIGNAL.AAG1598

15. van Tetering, G., & Vooijs, M. (2011). Proteolytic cleavage of Notch: "HIT and RUN". *Current molecular medicine*, *11*(4), 255–269. https://doi.org/10.2174/156652411795677972

16. Pan, L., Hoffmeister, P., Turkiewicz, A., Duyen Huynh, N. N., Große-berkenbusch, A., Knippschild, U., Gebhardt, J. C. M., Baumann, B., Borggrefe, T., & Oswald, F. (2021). Transcription factor rbpjl is able to repress notch target gene expression but is non-responsive to notch activation. *Cancers*, *13*(19), 5027. https://doi.org/10.3390/CANCERS13195027

17. Wang, H., et al. (2011). Genome-wide analysis reveals conserved and divergent features of Notch1/RBPJ binding in human and murine T-lymphoblastic leukemia cells. *Proceedings of the National Academy of Sciences of the United States of America*, *108*(36), 14908–14913. https://doi.org/10.1073/PNAS.1109023108

18. Lake, R. J., Tsai, P. F., Choi, I., Won, K. J., & Fan, H. Y. (2014). RBPJ, the Major Transcriptional Effector of Notch Signaling, Remains Associated with Chromatin throughout Mitosis, Suggesting a Role in Mitotic Bookmarking. *PLOS Genetics*, *10*(3), e1004204. https://doi.org/10.1371/JOURNAL.PGEN.1004204

19. Kovall, R. A. (2008). More complicated than it looks: assembly of Notch pathway transcription complexes. *Oncogene 2008 27:38*, *27*(38), 5099–5109. https://doi.org/10.1038/onc.2008.223

20. Arnett, K. L., Hass, M., McArthur, D. G., Ilagan, M. X. G., Aster, J. C., Kopan, R., & Blacklow, S. C. (2010). Structural and Mechanistic Insights into Cooperative Assembly of Dimeric Notch Transcription Complexes. *Nature Structural & Molecular Biology*, *17*(11), 1312-1317. https://doi.org/10.1038/NSMB.1938

21. Tong, X., Tang, R., Xu, J., Wang, W., Zhao, Y., Yu, X., & Shi, S. (2022). Liquid–liquid phase separation in tumor biology. *Signal Transduction and Targeted Therapy 2022 7:1*, *7*(1), 1–22. https://doi.org/10.1038/s41392-022-01076-x

22. Peng, P.H., Hsu, K.W., & Wu, K.J. (2021). Liquid-liquid phase separation (LLPS) in cellular physiology and tumor biology. *American Journal of Cancer Research*, *11*(8), 3766-3776. PMC:8414392

23. Wang, B., Zhang, L., Dai, T., Qin, Z., Lu, H., Zhang, L., & Zhou, F. (2021). Liquid–liquid phase separation in human health and diseases. *Signal Transduction and Targeted Therapy 2021 6:1*, *6*(1), 1–16. https://doi.org/10.1038/s41392-021-00678-1

24. Alberti, S., Gladfelter, A., & Mittag, T. (2019). Considerations and challenges in studying liquid-liquid phase separation and biomolecular condensates. *Cell*, *176*(3), 419-434. https://doi.org/10.1016/J.CELL.2018.12.035

25. Gao, Y., Li, X., Li, P., & Lin, Y. (2022). A brief guideline for studies of phase-separated biomolecular condensates. *Nature Chemical Biology*, *18*(12), 1307-1318. https://doi.org/10.1038/S41589-022-01204-2

26. Ganser, L. R., & Myong, S. (2020). Methods to Study Phase-Separated Condensates and the Underlying Molecular Interactions. *Trends in Biochemical Sciences*, *45*(11), 1004–1005. https://doi.org/10.1016/J.TIBS.2020.05.011

27. Martin, E. W., & Holehouse, A. S. (2020). Intrinsically disordered protein regions and phase separation: sequence determinants of assembly or lack thereof. *Emerging Topics in Life Sciences*, *4*(3), 307–329. https://doi.org/10.1042/ETLS20190164

28. Jo, Y., Jang, J., Song, D., Park, H., & Jung, Y. (2022). Determinants for intrinsically disordered protein recruitment into phase-separated protein condensates. *Chemical Science*, *13*(2), 522-530. https://doi.org/10.1039/D1SC05672G

29. Sabari, B. R., et al. (2018). Coactivator condensation at super-enhancers links phase separation and gene control. *Science*, *361*(6400). https://doi.org/10.1126/SCIENCE.AAR3958

30. Wei, M. T., Chang, Y. C., Shimobayashi, S. F., Shin, Y., Strom, A. R., & Brangwynne, C. P. (2020). Nucleated transcriptional condensates amplify gene expression. *Nature Cell Biology*, *22*(10), 1187–1196. https://doi.org/10.1038/S41556-020-00578-6

31. Sidor, C., Borreguero-Munoz, N., Fletcher, G. C., Elbediwy, A., Guillermin, O., & Thompson, B. J. (2019). Mask family proteins ankhd1 and ankrd17 regulate yap nuclear import and stability. *ELife*, *8*:e48601. https://doi.org/10.7554/elife.48601

32. Lu, Y., Wu, T., Gutman, O., Lu, H., Zhou, Q., Henis, Y. I., & Luo, K. (2020). Phase separation of TAZ compartmentalizes the transcription machinery to promote gene expression. *Nature Cell Biology*, *22*(4), 453–464. https://doi.org/10.1038/S41556-020-0485-0

33. Cai, D., Feliciano, D., Dong, P., Flores, E., Gruebele, M., Porat-Shliom, N., Sukenik, S., Liu, Z., & Lippincott-Schwartz, J. (2019). Phase separation of YAP reorganizes genome topology for long-term YAP target gene expression. *Nature Cell Biology 2019 21:12*, *21*(12), 1578–1589. https://doi.org/10.1038/s41556-019-0433-z

34. Erdős, G., & Dosztányi, Z. (2020). Analyzing Protein Disorder with IUPred2A. *Current Protocols in Bioinformatics*, *70*(1). https://doi.org/10.1002/CPBI.99

35. Mészáros, B., Erdös, G., & Dosztányi, Z. (2018). IUPred2A: context-dependent prediction of protein disorder as a function of redox state and protein binding. *Nucleic Acids Research*, *46*(W1), W329–W337. https://doi.org/10.1093/NAR/GKY384

36. Hallaq, R., et al. (2015). The Notch intracellular domain represses CRE-dependent transcription. *Cellular Signalling*, *27*(3), 621–629. https://doi.org/10.1016/j.cellsig.2014.11.034

37. Blain, J., Bédard, J., Thompson, M., Boisvert, F. M., & Boucher, M. J. (2017). C-terminal deletion of NOTCH1 intracellular domain (N1ICD) increases its stability but does not amplify and recapitulate N1ICD-dependent signalling. *Scientific Reports*, *7*(5034). https://doi.org/10.1038/s41598-017-05119-0

38. Petrovic, J., Zhou, Y., Fasolino, M., Vahedi, G., Pear, W. S., & Faryabi Correspondence, R. B. (2019). Oncogenic Notch Promotes Long-Range Regulatory Interactions within Hyperconnected 3D Cliques. *Molecular Cell*, *73, 1174-1190*. https://doi.org/10.1016/j.molcel.2019.01.006

39. Jumper, J., et al. (2021). Highly accurate protein structure prediction with AlphaFold. *Nature 2021 596:7873*, *596*(7873), 583–589. https://doi.org/10.1038/s41586-021-03819-2

40. Varadi, M., et al. (2022). AlphaFold Protein Structure Database: massively expanding the structural coverage of protein-sequence space with high-accuracy models. *Nucleic Acids Research*, *50*(D1), D439–D444. https://doi.org/10.1093/NAR/GKAB1061

41. Lancaster, A. K., Nutter-Upham, A., Lindquist, S., & King, O. D. (2014). PLAAC: a web and command-line application to identify proteins with prion-like amino acid composition. *Bioinformatics (Oxford, England)*, *30*(17), 2501–2502. https://doi.org/10.1093/BIOINFORMATICS/BTU310

42. Holehouse, A. S., Das, R. K., Ahad, J. N., Richardson, M. O. G., & Pappu, R. v. (2017). CIDER: Resources to Analyze Sequence-Ensemble Relationships of Intrinsically Disordered Proteins. *Biophysical Journal*, *112*(1), 16–21. https://doi.org/10.1016/J.BPJ.2016.11.3200

43. Sherry, K. P., Das, R. K., Pappu, R. v., & Barrick, D. (2017). Control of transcriptional activity by design of charge patterning in the intrinsically disordered RAM region of the Notch receptor. *Proceedings of the National Academy of Sciences of the United States of America*, *114*(44), E9243–E9252. https://doi.org/10.1073/PNAS.1706083114

44. Tamura, K., Taniguchi, Y., Minoguchi, S., Sakai, T., Tun, T., Furukawa, T., & Honjo, T. (1995). Physical interaction between a novel domain of the receptor Notch and the transcription factor RBP-J kappa/Su(H). *Current Biology□: CB*, *5*(12), 1416–1423. https://doi.org/10.1016/S0960-9822(95)00279-X

45. Chen, N., Zhao, Z., Wang, Y., & Dimova, R. (2020). Resolving the Mechanisms of Soy Glycinin Self-Coacervation and Hollow-Condensate Formation. *ACS Macro Letters*, *9*(12), 1844–1852. https://doi.org/10.1021/ACSMACROLETT.0C00709

46. Alshareedah, I., Moosa, M. M., Raju, M., Potoyan, D. A., & Banerjee, P. R. (2020). Phase transition of RNA−protein complexes into ordered hollow condensates. *Proceedings of*

the National Academy of Sciences of the United States of America, *117*(27), 15650–15658. https://doi.org/10.1073/PNAS.1922365117

47. Düster, R., Kaltheuner, I. H., Schmitz, M., & Geyer, M. (2021). 1,6-Hexanediol, commonly used to dissolve liquid-liquid phase separated condensates, directly impairs kinase and phosphatase activities. *Journal of Biological Chemistry*, *296*, 100260–100261. https://doi.org/10.1016/J.JBC.2021.100260

48. Uhlén, M., et al. (2015). Tissue-based map of the human proteome. *Science*, *347*(6220). https://doi.org/10.1126/SCIENCE.1260419

49. Lee, D., Creed, M., Jung, K., Stefanelli, T., Wendler, D. J., Oh, W. C., Mignocchi, N. L., Lüscher, C., & Kwon, H.-B. (2017). Temporally precise labeling and control of neuromodulatory circuits in the mammalian brain. *Nat Methods 14*(5), 495-503. https://doi.org/10.1038/nmeth.4234

50. Taslimi, A., Zoltowski, B., Miranda, J. G., Pathak, G., Hughes, R. M., & Tucker, C. L. (2016). Optimized second-generation CRY2–CIB dimerizers and photoactivatable Cre recombinase. *Nat Chem Biol. 12,425-430* https://doi.org/10.1038/nchembio.2063

51. Cesaratto, F., López-Requena, A., Burrone, O. R., & Petris, G. (2015). Engineered tobacco etch virus (TEV) protease active in the secretory pathway of mammalian cells. *Journal of Biotechnology*, *212*, 159–166. https://doi.org/10.1016/J.JBIOTEC.2015.08.026

52. Pudasaini, A., El-Arab, K. K., & Zoltowski, B. D. (2015). LOV-based optogenetic devices: light-driven modules to impart photoregulated control of cellular signaling. *Frontiers in Molecular Biosciences*, *2*, 18. https://doi.org/10.3389/FMOLB.2015.00018

53. Kennedy, M. J., Hughes, R. M., Peteya, L. A., Schwartz, J. W., Ehlers, M. D., & Tucker, C. L. (2010). Rapid blue-light-mediated induction of protein interactions in living cells. *Nature Methods*, *7*(12), 973–975. https://doi.org/10.1038/nmeth.1524

54. Monahan, P., Rybak, S., & Raetzman, L. T. (2009). The notch target gene HES1 regulates cell cycle inhibitor expression in the developing pituitary. *Endocrinology*, *150*(9), 4386–4394. https://doi.org/10.1210/EN.2009-0206

55. Phair, R. D., & Misteli, T. (2001). Kinetic modelling approaches to in vivo imaging. *Nature Reviews. Molecular Cell Biology*, *2*(12), 898–907. https://doi.org/10.1038/35103000

56. Reits, E. A. J., & Neefjes, J. J. (2001). From fixed to FRAP: measuring protein mobility and activity in living cells. *Nature Cell Biology*, *3*(6), E145–E145. https://doi.org/10.1038/35078615

57. Rhine, K., Skanchy, S., & Myong, S. (2022). Single-molecule and ensemble methods to probe RNP nucleation and condensate properties. *Methods*, *197*, 74–81. https://doi.org/10.1016/J.YMETH.2021.02.012

58. Culley, S., Albrecht, D., Jacobs, C., Pereira, P. M., Leterrier, C., Mercer, J., & Henriques, R. (2018). NanoJ-SQUIRREL: quantitative mapping and minimisation of super-resolution optical imaging artefacts. *Nature Methods*, *15*(4), 263-266. https://doi.org/10.1038/NMETH.4605

59. Gustafsson, N., Culley, S., Ashdown, G., Owen, D. M., Pereira, P. M., & Henriques, R. (2016). Fast live-cell conventional fluorophore nanoscopy with ImageJ through super-resolution

radial fluctuations. *Nature Communications 2016 7:1*, *7*(1), 1–9. https://doi.org/10.1038/ncomms12471

60. Culley, S., Tosheva, K. L., Matos Pereira, P., & Henriques, R. (2018). SRRF: Universal live-cell super-resolution microscopy. *International Journal of Biochemistry and Cell Biology.* 101, 74-79. Elsevier Ltd. https://doi.org/10.1016/j.biocel.2018.05.014

61. Donato, E., Croci, O., Sabò, A., Muller, H., Morelli, M. J., Pelizzola, M., & Campaner, S. (2017). Compensatory RNA polymerase 2 loading determines the efficacy and transcriptional selectivity of JQ1 in Myc-driven tumors. *Leukemia*, *31*(2), 479-490. https://doi.org/10.1038/LEU.2016.182

62. Lancho, O., & Herranz, D. (2018). The MYC enhancer-ome: Long-range transcriptional regulation of MYC. *Trends in Cancer*, *4*(12), 810-822. https://doi.org/10.1016/J.TRECAN.2018.10.003

63. Weng, A. P., et al. (2006). c-Myc is an important direct target of Notch1 in T-cell acute lymphoblastic leukemia/lymphoma. *Genes & Development*, 20, 2096-2109. https://doi.org/10.1101/gad.1450406

64. Palomero, T., et al. (2006). NOTCH1 directly regulates c-MYC and activates a feed-forward-loop transcriptional network promoting leukemic cell growth. *Proceedings of the National Academy of Sciences of the United States of America*, *103*(48), 18261–18266. https://doi.org/10.1073/PNAS.0606108103/

65. Lu, H., Jiang, J., & Gao, Y. (2018). The cloning and activity of human Hes1 gene promoter. *Molecular Medicine Reports*, *17*(2), 3164–3169. https://doi.org/10.3892/MMR.2017.8240/HTML

66. Tutucci, E., Vera, M., Biswas, J., Garcia, J., Parker, R., & Singer, R. H. (2018). An improved MS2 system for accurate reporting of the mRNA life cycle. *Nature Methods*, *15*(1), 81-89. https://doi.org/10.1038/NMETH.4502

67. Zhao, S., Jiang, E., Chen, S., Gu, Y., Shangguan, A. J., Lv, T., Luo, L., & Yu, Z. (2016). PiggyBac transposon vectors: the tools of the human gene encoding. *Translational Lung Cancer Research*, *5*(1), 120-125. https://doi.org/10.3978/J.ISSN.2218-6751.2016.01.05

68. Beliveau, B. J., Boettiger, A. N., Nir, G., Bintu, B., Yin, P., Zhuang, X., & Wu, C. ting. (2017). In Situ Super-Resolution Imaging of Genomic DNA with OligoSTORM and OligoDNA-PAINT. *Methods in Molecular Biology (Clifton, N.J.)*, *1663*, 231–252. https://doi.org/10.1007/978-1-4939-7265-4_19

69. Hagege, H., Klous, P., Braem, C., Splinter, E., Dekker, J., Cathala, G., de Laat, W., & Forne, T. (2007). Quantitative analysis of chromosome conformation capture assays (3C-qPCR). *Nature Protocols 2007 2:7*, *2*(7), 1722–1733. https://doi.org/10.1038/nprot.2007.243

70. Schilit, S. L. P., & Morton, C. C. (2018). 3C-PCR: a novel proximity ligation-based approach to phase chromosomal rearrangement breakpoints with distal allelic variants. *Human Genetics*, *137*(1), 55–62. https://doi.org/10.1007/S00439-017-1853-0

71. Hnisz, D., Shrinivas, K., Young, R. A., Chakraborty, A. K., & Sharp, P. A. (2017). A phase separation model predicts key features of transcriptional control. *Cell*, *169*(1), 13-23. https://doi.org/10.1016/J.CELL.2017.02.007

72. Ghavi-Helm, Y., Jankowski, A., Meiers, S., Viales, R. R., Korbel, J. O., & Furlong, E. E. M. (2019). Highly rearranged chromosomes reveal uncoupling between genome topology and gene expression. *Nature Genetics 2019 51:8*, *51*(8), 1272–1282. https://doi.org/10.1038/s41588-019-0462-3

73. Mir, M., Bickmore, W., Furlong, E. E. M., & Narlikar, G. (2019). Chromatin topology, condensates and gene regulation: shifting paradigms or just a phase?, *146*(19), 1-6. https://doi.org/10.1242/DEV.182766

74. Sladitschek, H. L., Neveu, P. A., Chellappan, S. P., & Lee, H. (2015). MXS-Chaining: A Highly Efficient Cloning Platform for Imaging and Flow Cytometry Approaches in Mammalian Systems. *PLOS ONE*, *10*(4), e0124958. https://doi.org/10.1371/JOURNAL.PONE.0124958

75. Dickson, E. J., Jensen, J. B., & Hille, B. (2014). Golgi and plasma membrane pools of PI(4)P contribute to plasma membrane PI(4,5)P2 and maintenance of KCNQ2/3 ion channel current. *Proceedings of the National Academy of Sciences of the United States of America*, *111*(22), E2281–E2290. https://doi.org/10.1073/PNAS.1407133111

76. Voorde, J. vande, Ackermann, T., Pfetzer, N., Sumpton, D., Mackay, G., Kalna, G., Nixon, C., Blyth, K., Gottlieb, E., & Tardito, S. (2019). Improving the metabolic fidelity of cancer models with a physiological cell culture medium. *Science Advances*, *5*(1). https://doi.org/10.1126/SCIADV.AAU7314/

77. Li, Q., Kim, Y., Namm, J., Kulkarni, A., Rosania, G. R., Ahn, Y. H., & Chang, Y. T. (2006). RNA-selective, live cell imaging probes for studying nuclear structure and function. *Chemistry & Biology*, *13*(6), 615–623. https://doi.org/10.1016/J.CHEMBIOL.2006.04.007

78. Wilk, R., Hu, J., & Krause, H. M. (2017). In Situ Hybridization: Fruit Fly Embryos and Tissues. *Current Protocols Essential Laboratory Techniques*, *15*(1), 9.3.1-9.3.26. https://doi.org/10.1002/CPET.14

79. Abraham, M., et al. (2023). *GROMACS 2023 Manual*. https://doi.org/10.5281/ZENODO.7588711

80. Páll, S., Zhmurov, A., Bauer, P., Abraham, M., Lundborg, M., Gray, A., Hess, B., & Lindahl, E. (2020). Heterogeneous parallelization and acceleration of molecular dynamics simulations in GROMACS. *The Journal of Chemical Physics*, *153*(13), 134110. https://doi.org/10.1063/5.0018516

81. Humphrey, W., Dalke, A., & Schulten, K. (1996). VMD: Visual molecular dynamics. *Journal of Molecular Graphics*, *14*(1), 33–38. https://doi.org/10.1016/0263-7855(96)00018-5

82. Yashiro-Ohtani, Y., et al. (2014). Long-range enhancer activity determines Myc sensitivity to Notch inhibitors in T cell leukemia. *Proceedings of the National Academy of Sciences of the United States of America*, *111*(46), E4946–E4953. https://doi.org/10.1073/PNAS.1407079111

83. Schneider, C. A., Rasband, W. S., & Eliceiri, K. W. (2012). NIH Image to ImageJ: 25 years of image analysis. *Nature Methods 2012 9:7*, *9*(7), 671–675. https://doi.org/10.1038/nmeth.2089

84. RStudio Team. (2020). *RStudio: Integrated Development for R.* RStudio, PBC. http://www.rstudio.com/

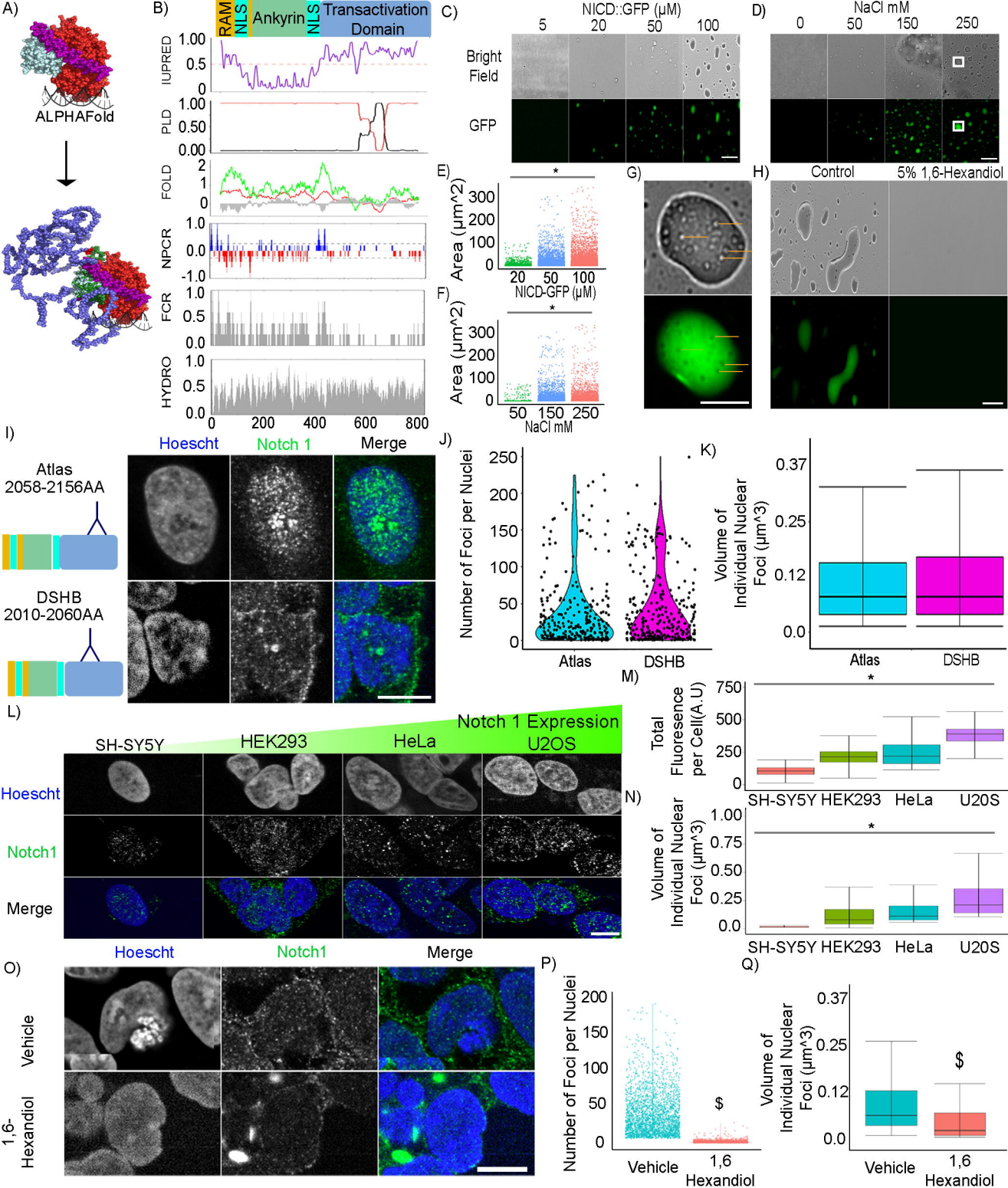
A)
ALPHAFold
B)
RAM
NLS
Ankyrin
NLS
Transactivation Domain
IUPRED
PLD
FOLD
NPCR
FCR
HYDRO
0
200
400
600
800
C)
NICD::GFP (μM)
5
20
50
100
Bright Field
GFP
D)
NaCl mM
0
50
150
250
E)
Area (μm^2)
NICD-GFP (μM)
F)
Area (μm^2)
NaCl mM
G)
H)
Control
5% 1,6-Hexandiol
I)
Hoescht
Notch 1
Merge
Atlas
2058-2156AA
DSHB
2010-2060AA
J)
Number of Foci per Nuclei
Atlas
DSHB
K)
Volume of Individual Nuclear Foci (μm^3)
Atlas
DSHB
L)
SH-SY5Y
HEK293
HeLa
U2OS
Notch 1 Expression
Hoescht
Notch1
Merge
M)
Total Fluoresence per Cell(A.U)
SH-SY5Y
HEK293
HeLa
U2OS
N)
Volume of Individual Nuclear Foci (μm^3)
SH-SY5Y
HEK293
HeLa
U2OS
O)
Hoescht
Notch1
Merge
Vehicle
1,6-Hexandiol
P)
Number of Foci per Nuclei
Vehicle
1,6 Hexandiol
Q)
Volume of Individual Nuclear Foci (μm^3)
Vehicle
1,6 Hexandiol

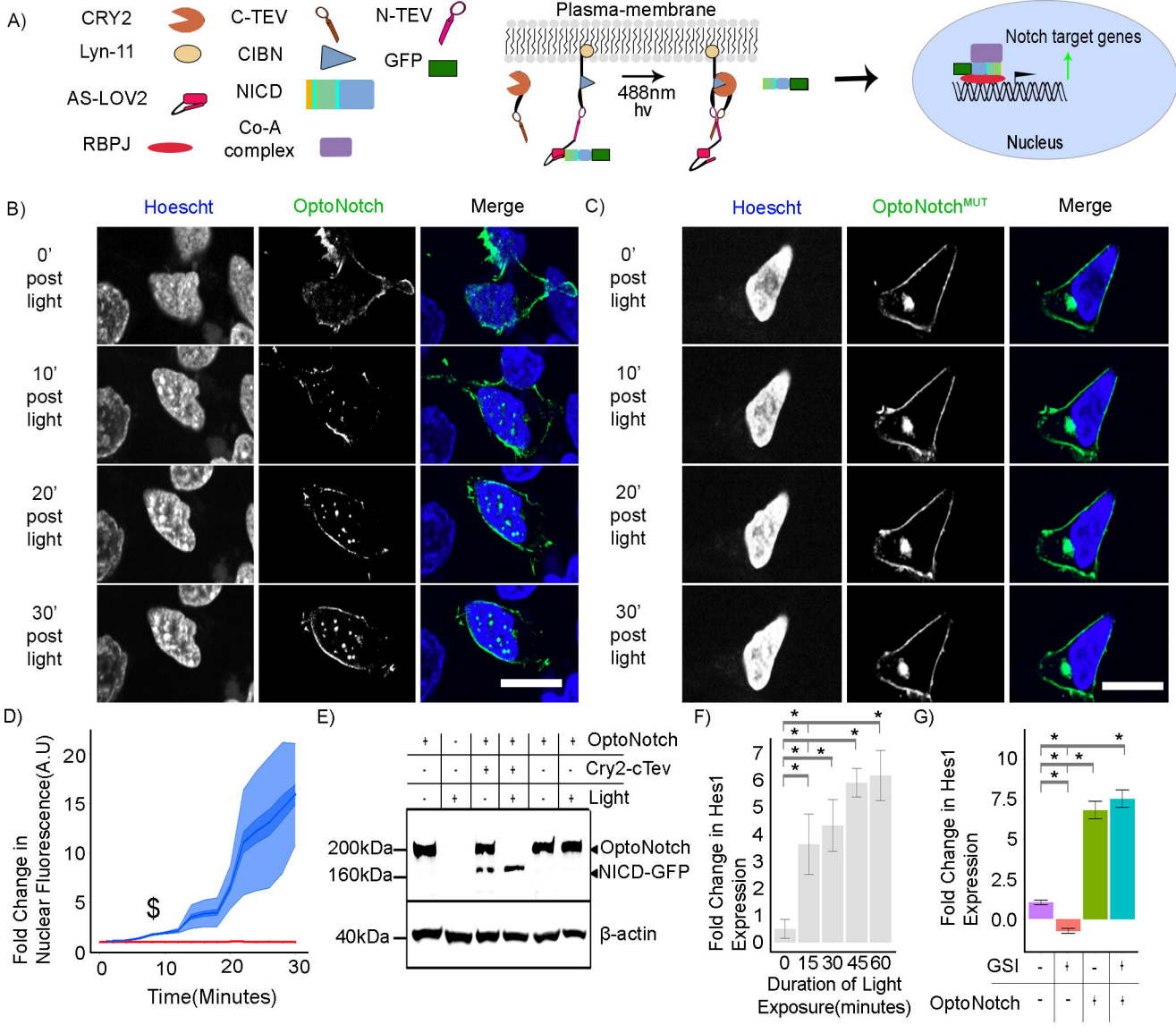
A)
CRY2
C-TEV
N-TEV
Lyn-11
CIBN
GFP
AS-LOV2
NICD
RBPJ
Co-A complex
Plasma-membrane
488nm hv
Notch target genes
Nucleus
B)
Hoescht
OptoNotch
Merge
C)
Hoescht
OptoNotch^MUT
Merge
0' post light
10' post light
20' post light
30' post light
D)
Fold Change in Nuclear Fluorescence(A.U)
Time(Minutes)
$
E)
OptoNotch
Cry2-cTev
Light
200kDa
160kDa
OptoNotch
NICD-GFP
40kDa
β-actin
F)
Fold Change in Hes1 Expression
Duration of Light Exposure(minutes)
G)
Fold Change in Hes1 Expression
GSI
OptoNotch

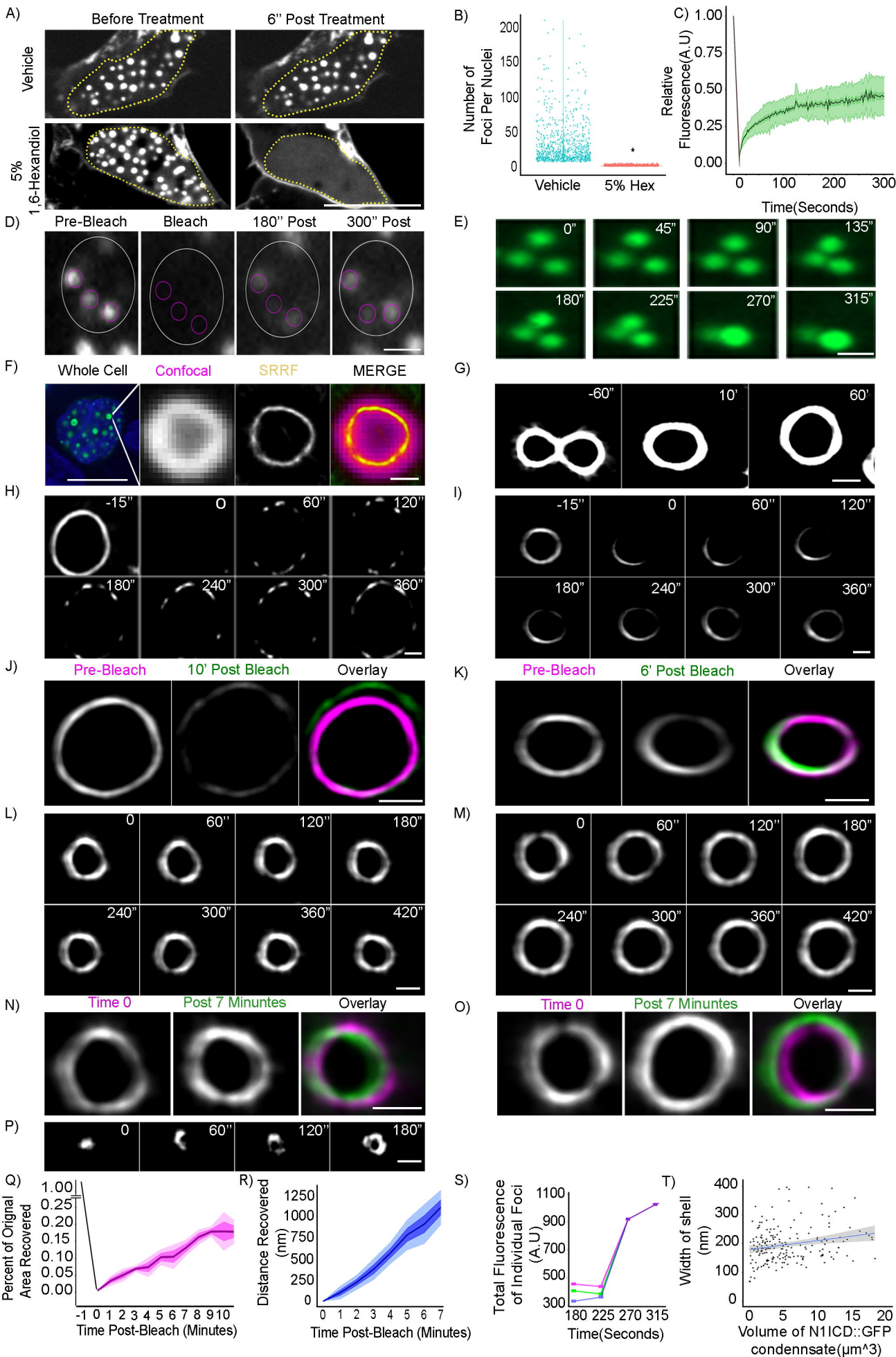
A)
Before Treatment
6'' Post Treatment
Vehicle
5% 1,6-Hexandiol
B)
Number of Foci Per Nuclei
Vehicle
5% Hex
C)
Relative Fluorescence(A.U)
Time(Seconds)
D)
Pre-Bleach
Bleach
180'' Post
300'' Post
E)
0''
45''
90''
135''
180''
225''
270''
315''
F)
Whole Cell
Confocal
SRRF
MERGE
G)
-60''
10'
60'
H)
-15''
0
60''
120''
180''
240''
300''
360''
I)
-15''
0
60''
120''
180''
240''
300''
360''
J)
Pre-Bleach
10' Post Bleach
Overlay
K)
Pre-Bleach
6' Post Bleach
Overlay
L)
0
60''
120''
180''
240''
300''
360''
420''
M)
0
60''
120''
180''
240''
300''
360''
420''
N)
Time 0
Post 7 Minuntes
Overlay
O)
Time 0
Post 7 Minuntes
Overlay
P)
0
60''
120''
180''
Q)
Percent of Orignal Area Recovered
Time Post-Bleach (Minutes)
R)
Distance Recovered (nm)
Time Post-Bleach (Minutes)
S)
Total Fluorescence of Individual Foci (A.U)
Time(Seconds)
T)
Width of shell (nm)
Volume of N1ICD::GFP condennsate(μm^3)

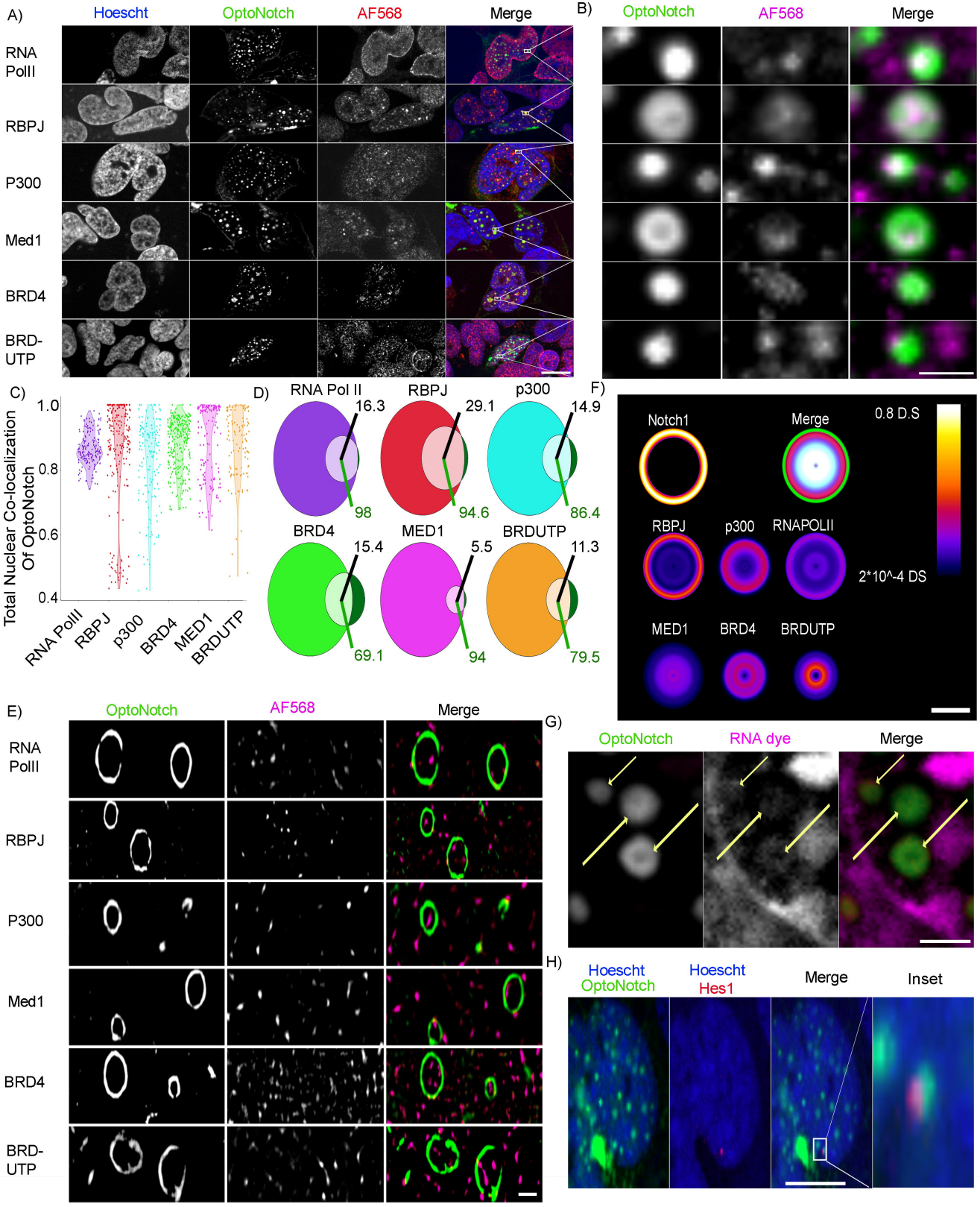
A)
Hoescht
OptoNotch
AF568
Merge
RNA PolII
RBPJ
P300
Med1
BRD4
BRD-UTP
B)
OptoNotch
AF568
Merge
C)
Total Nuclear Co-localization Of OptoNotch
1.0
0.8
0.6
0.4
RNA PolII
RBPJ
p300
BRD4
MED1
BRDUTP
D)
RNA Pol II
16.3
98
RBPJ
29.1
94.6
p300
14.9
86.4
BRD4
15.4
69.1
MED1
5.5
94
BRDUTP
11.3
79.5
F)
Notch1
Merge
0.8 D.S
RBPJ
p300
RNAPOLII
2*10^-4 DS
MED1
BRD4
BRDUTP
E)
OptoNotch
AF568
Merge
RNA PolII
RBPJ
P300
Med1
BRD4
BRD-UTP
G)
OptoNotch
RNA dye
Merge
H)
Hoescht
OptoNotch
Hoescht
Hes1
Merge
Inset

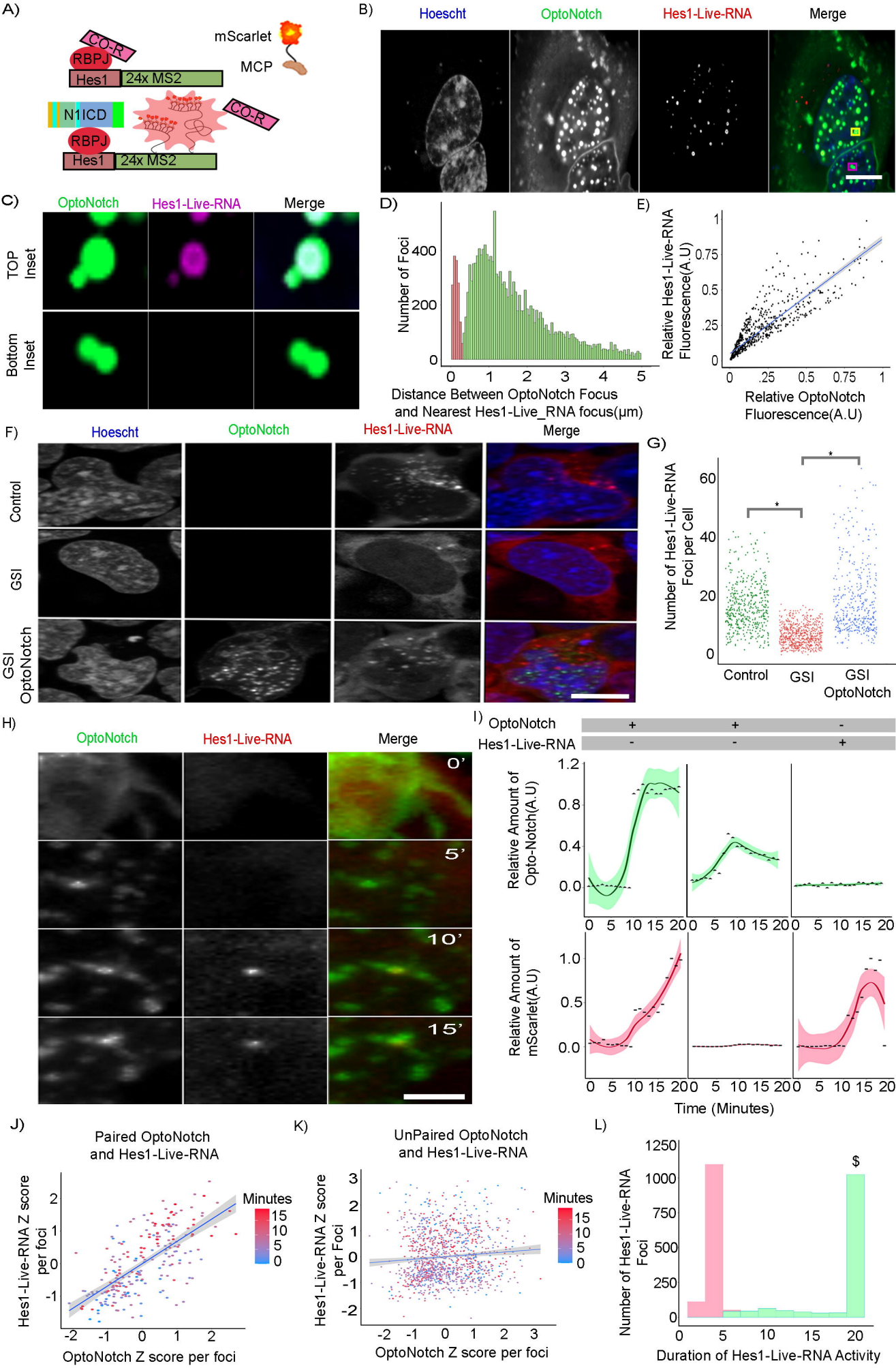
A)
CO-R
RBPJ
Hes1
24x MS2
mScarlet
MCP
N1ICD
CO-R
RBPJ
Hes1
24x MS2
B)
Hoescht
OptoNotch
Hes1-Live-RNA
Merge
C)
OptoNotch
Hes1-Live-RNA
Merge
TOP Inset
Bottom Inset
D)
Number of Foci
Distance Between OptoNotch Focus and Nearest Hes1-Live_RNA focus(μm)
E)
Relative Hes1-Live-RNA Fluorescence(A.U)
Relative OptoNotch Fluorescence(A.U)
F)
Hoescht
OptoNotch
Hes1-Live-RNA
Merge
Control
GSI
GSI OptoNotch
G)
Number of Hes1-Live-RNA Foci per Cell
Control
GSI
GSI OptoNotch
H)
OptoNotch
Hes1-Live-RNA
Merge
0'
5'
10'
15'
I)
OptoNotch
Hes1-Live-RNA
Relative Amount of Opto-Notch(A.U)
Relative Amount of mScarlet(A.U)
Time (Minutes)
J)
Paired OptoNotch and Hes1-Live-RNA
Hes1-Live-RNA Z score per foci
OptoNotch Z score per foci
Minutes
K)
UnPaired OptoNotch and Hes1-Live-RNA
Hes1-Live-RNA Z score per Foci
OptoNotch Z score per foci
Minutes
L)
Number of Hes1-Live-RNA Foci
Duration of Hes1-Live-RNA Activity

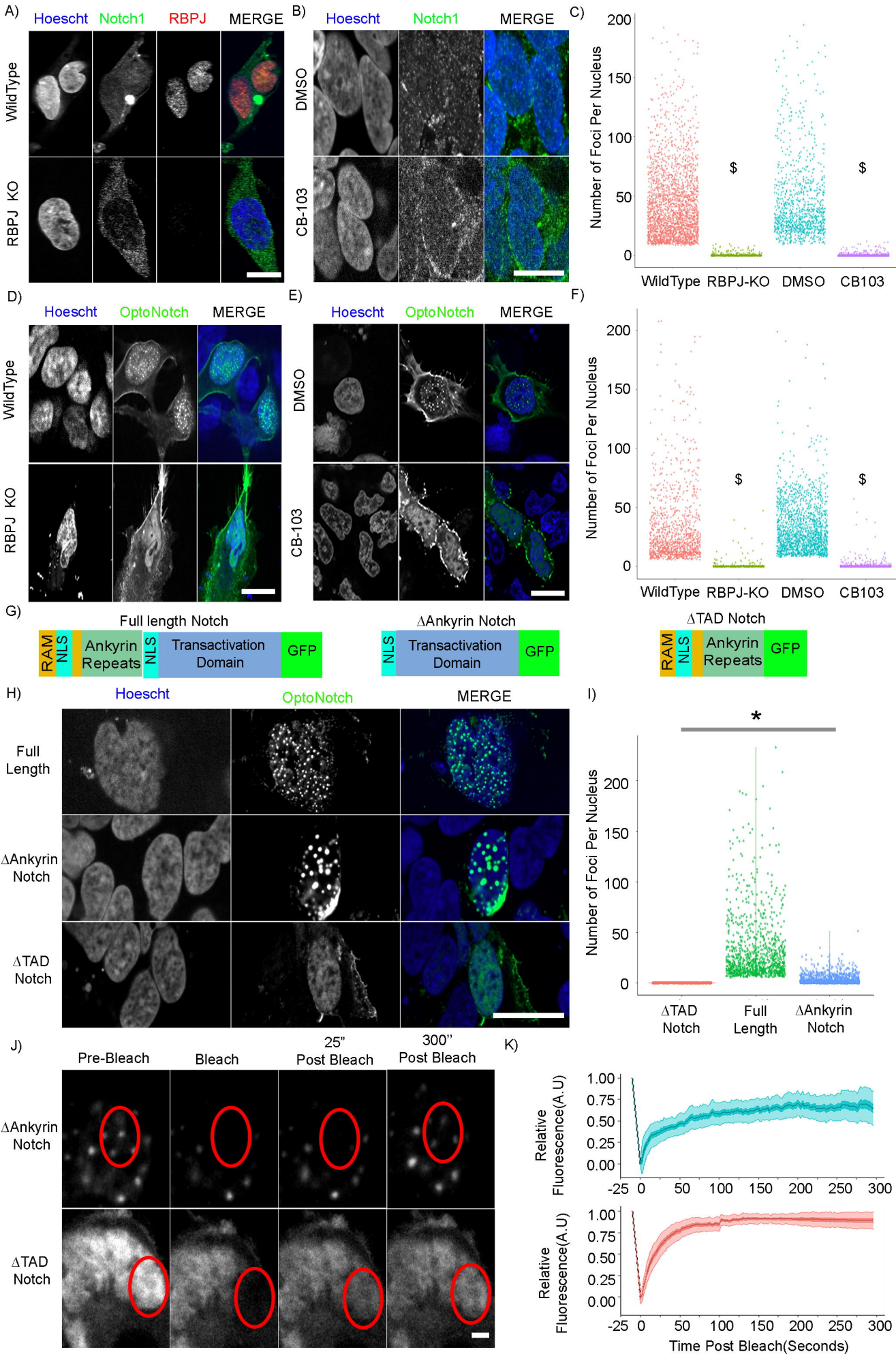
A)
Hoescht
Notch1
RBPJ
MERGE
WildType
RBPJ KO
B)
Hoescht
Notch1
MERGE
DMSO
CB-103
C)
Number of Foci Per Nucleus
200
150
100
50
0
$
$
WildType
RBPJ-KO
DMSO
CB103
D)
Hoescht
OptoNotch
MERGE
WildType
RBPJ KO
E)
Hoescht
OptoNotch
MERGE
DMSO
CB-103
F)
Number of Foci Per Nucleus
200
150
100
50
0
$
$
WildType
RBPJ-KO
DMSO
CB103
G)
Full length Notch
RAM
NLS
Ankyrin Repeats
NLS
Transactivation Domain
GFP
ΔAnkyrin Notch
NLS
Transactivation Domain
GFP
ΔTAD Notch
RAM
NLS
Ankyrin Repeats
GFP
H)
Hoescht
OptoNotch
MERGE
Full Length
ΔAnkyrin Notch
ΔTAD Notch
I)
*
Number of Foci Per Nucleus
200
150
100
50
0
ΔTAD Notch
Full Length
ΔAnkyrin Notch
J)
Pre-Bleach
Bleach
25" Post Bleach
300" Post Bleach
ΔAnkyrin Notch
ΔTAD Notch
K)
Relative Fluorescence(A.U)
1.00
0.75
0.50
0.25
0.00
-25
0
50
100
150
200
250
300
Relative Fluorescence(A.U)
1.00
0.75
0.50
0.25
0.00
-25
0
50
100
150
200
250
300
Time Post Bleach(Seconds)

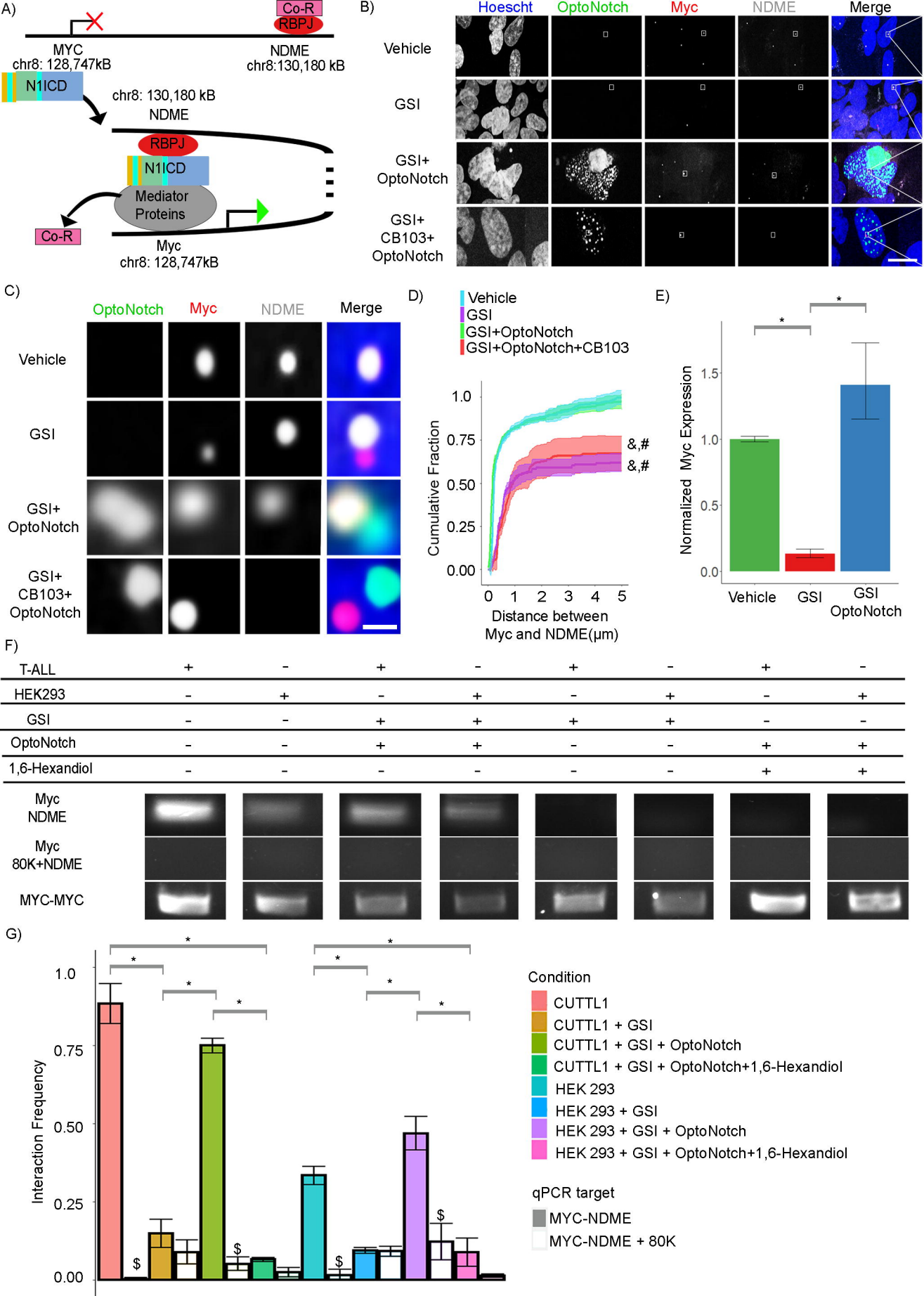
A)
Co-R
RBPJ
MYC
chr8: 128,747kB
NDME
chr8:130,180 kB
N1ICD
chr8: 130,180 kB
NDME
RBPJ
N1ICD
Mediator
Proteins
Co-R
Myc
chr8: 128,747kB
B)
Hoescht
OptoNotch
Myc
NDME
Merge
Vehicle
GSI
GSI+
OptoNotch
GSI+
CB103+
OptoNotch
C)
OptoNotch
Myc
NDME
Merge
Vehicle
GSI
GSI+
OptoNotch
GSI+
CB103+
OptoNotch
D)
Vehicle
GSI
GSI+OptoNotch
GSI+OptoNotch+CB103
Cumulative Fraction
1.0
0.75
0.50
0.25
0.00
0 1 2 3 4 5
Distance between
Myc and NDME(μm)
&,#
&,#
E)
Normalized Myc Expression
1.5
1.0
0.5
0.0
Vehicle
GSI
GSI
OptoNotch
F)
T-ALL + - + - + - + -
HEK293 - + - + - + - +
GSI - - + + + + - -
OptoNotch - - + + - - + +
1,6-Hexandiol - - - - - - + +
Myc
NDME
Myc
80K+NDME
MYC-MYC
G)
Interaction Frequency
1.0
0.75
0.50
0.25
0.00
Condition
CUTTL1
CUTTL1 + GSI
CUTTL1 + GSI + OptoNotch
CUTTL1 + GSI + OptoNotch+1,6-Hexandiol
HEK 293
HEK 293 + GSI
HEK 293 + GSI + OptoNotch
HEK 293 + GSI + OptoNotch+1,6-Hexandiol
qPCR target
MYC-NDME
MYC-NDME + 80K